



## Using river hypsometry to improve remote sensing of river discharge

Michael Durand<sup>a,b</sup>, Chunli Dai<sup>c</sup>, Joachim Moortgat<sup>a</sup>, Bidhyananda Yadav<sup>b,\*</sup>, Renato Prata de Moraes Frasson<sup>d</sup>, Ziwei Li<sup>e</sup>, Kylie Wadkwoski<sup>f</sup>, Ian Howat<sup>a,b</sup>, Tamlin M. Pavelsky<sup>g</sup>

<sup>a</sup> School of Earth Sciences, Ohio State University, Columbus, OH 43210, USA

<sup>b</sup> Byrd Polar and Climate Research Center, Ohio State University, Columbus, OH 43210, USA

<sup>c</sup> School of Forest, Fisheries, and Geomatics Sciences (FFGS), University of Florida, Gainesville, FL, USA

<sup>d</sup> Jet Propulsion Laboratory, California Institute of Technology, Pasadena, CA 91109, USA

<sup>e</sup> Computer Science and Engineering, Ohio State University, Columbus, OH 43210, USA

<sup>f</sup> Doerr School of Sustainability, Stanford University, Stanford, CA 94305, USA

<sup>g</sup> Department of Earth, Marine and Environmental Sciences, University of North Carolina, Chapel Hill, NC, USA

### ARTICLE INFO

Editor: Dr. Menghua Wang

**Keywords:**

Remote sensing  
Hydrology  
Rivers  
Discharge  
River width  
Water surface elevation  
SWOT

### ABSTRACT

Remote sensing has the potential to dramatically advance river discharge monitoring globally, but precision of primary data (water surface elevation (WSE) and river width) remains a limiting factor. WSE can be measured from altimeters, and river width from imagers, but the measurements historically have not been made concurrently from space. This is changing with the advent of the Surface Water and Ocean Topography (SWOT) mission and is anticipated by the combination of high-resolution commercial imagery and DEMs from ArcticDEM. WSE and width respond to changing flow conditions as modulated by the three-dimensional structure of the river channel bed and banks. The relationship between WSE and width thus increases monotonically and is essentially the hypsometric curve of the river. In this study, we explore how simultaneous measurements of WSE and width, combined with the monotonic nature of the river hypsometric curve, can be used to improve measurements of river discharge. First, we present an algorithm to compute the river hypsometric curve from noisy measurements of WSE and width. Second, we demonstrate a method to compute estimates of WSE and width constrained to the river hypsometric curve, and we analyze the probability distribution function of the hypsometrically constrained WSE and width estimates. Specifically, we show that the variance of width and WSE is reduced by invoking a hypsometric constraint, at the cost of an induced correlation between the WSE and width errors. Third, we show that river discharge estimated with the hypsometrically constrained WSE and width is more precise than that without hypsometric constraint, and we predict the expected reduction in discharge error. Fourth, we look at six example river reaches measured by ArcticDEM. The WSE root mean square error had a median across the six reaches of 39.3 cm, which was improved to 33.4 cm across the six reaches using the hypsometric constraint. The discharge predictions were similarly improved: the constrained height and width produce more accurate discharge estimates for five of the six reaches and show reduced variation among flow laws. With the launch of SWOT, river hypsometry constraints applied to simultaneous measurement of WSE and width will support new discharge estimates globally.

### 1. Introduction

New remote sensing technologies are enabling novel capabilities for monitoring global river discharge. Given the increasing scarcity of in situ global gage observations (Hannah et al., 2011), remote sensing of rivers is an alternative with immense potential. Despite much recent

progress (e.g. Gleason and Durand, 2020), remote sensing of discharge currently leverages sub-optimal instruments of opportunity. For example, one commonly used approach (typically suitable only for the largest rivers) measures river elevations using radar altimeters designed to measure ocean surfaces (Coss et al., 2020) and leverages fortuitous concurrent visible band imagery acquisitions to estimate river discharge

\* Corresponding author.

E-mail address: [yadav.111@osu.edu](mailto:yadav.111@osu.edu) (B. Yadav).

(Bjerkli et al., 2018). In all of these approaches to remote sensing of discharge, an important distinction is whether one is calibrating remotely sensed measurements to gaged discharge (Bjerkli et al., 2018) or inferring discharge by invoking more complex algorithms such as Mass-Conserved Flow Law Inversion (Frasson et al., 2021) to estimate discharge in ungaged basins. The former approach is only useful where gaged discharge measurements already exist, whereas the latter approach has the potential to estimate discharge in truly ungaged basins. No fewer than 168 relevant manuscripts on these topics are reviewed by Gleason and Durand (2020), and we do not attempt additional literature review here. While several papers have indeed been published since that review, the summary of Gleason and Durand (2020) is still relevant. Most existing methods suffer from i) low spatial resolution or posting of measurements, relative to the size of the rivers under study; and ii) a lack of concurrent measurements of both river water surface elevation and width. These data limitations pose important challenges for measuring river discharge for periods prior to the advent of the Surface Water and Ocean Topography (SWOT) satellite mission (<https://swot.jpl.nasa.gov>), which measures both width and water surface elevation. High-resolution commercial satellite imagery has the potential to fill these gaps in remote sensing of rivers, as demonstrated by Dai et al. (2018), by intersecting riverine water masks with elevation models produced via photogrammetry methods at high spatial resolution.

WSE and width respond to changing flow conditions as modulated by the three-dimensional structure of the river's bed and banks, which we refer to as the bathymetry (Fig. 1a). In this study we extend the concept of hypsometry to rivers. The hypsometric curve of the global land surface is commonly used to reflect the distribution of global land areas at various elevations above sea level. Hypsometric curves are commonly used in lake studies to relate lake elevation to lake area and thus compute lake storage variations from remote sensing measurements

(Cretaux et al., 2015; Tortini et al., 2020). Similarly, the relationship between WSE and width in rivers is monotonic increasing and is essentially the river hypsometric curve (Fig. 1c). Indeed, integration of the river hypsometric curve produces river cross-sectional area. While these principles have been used in remote sensing of discharge applications (e.g. Coss et al., 2023), they have been hindered by the lack of simultaneous WSE and width observations. In this study, we explore how simultaneous measurements of WSE and width, combined with the monotonic nature of the river hypsometric curve in natural rivers, can be used to improve measurements of river discharge. Specifically, we predict discharge using the spaceborne WSE and width measurements with and without constraint to a hypsometric curve. To isolate the effect of the flow law and observation error, flow law parameters are computed via calibration to gaged discharge in an attempt.

## 2. Analytical computations

In this section, we describe estimation of hypsometric curves and show that constraining WSE and width measurements to the hypsometric curve can enable more precise discharge predictions. As noted above, the river hypsometric curve is the relationship between WSE and width. New satellite measurements enable simultaneous measurements of WSE and width,  $H_t$  and  $W_t$  respectively, and their corresponding error standard deviations  $\sigma_H$  and  $\sigma_W$ . We here use the errors-in-variables model (Fuller, 1987) to estimate hypsometric curves, allowing for both WSE and width uncertainty, and we allow the hypsometric curves to be continuous, piece-wise linear functions. As a starting point, we consider a linear relationship for width as a function of WSE:

$$W_t = p_0 + p_1 H_t + e_t \quad (1)$$

where  $p_0$  and  $p_1$  are the parameters describing the linear relationship,

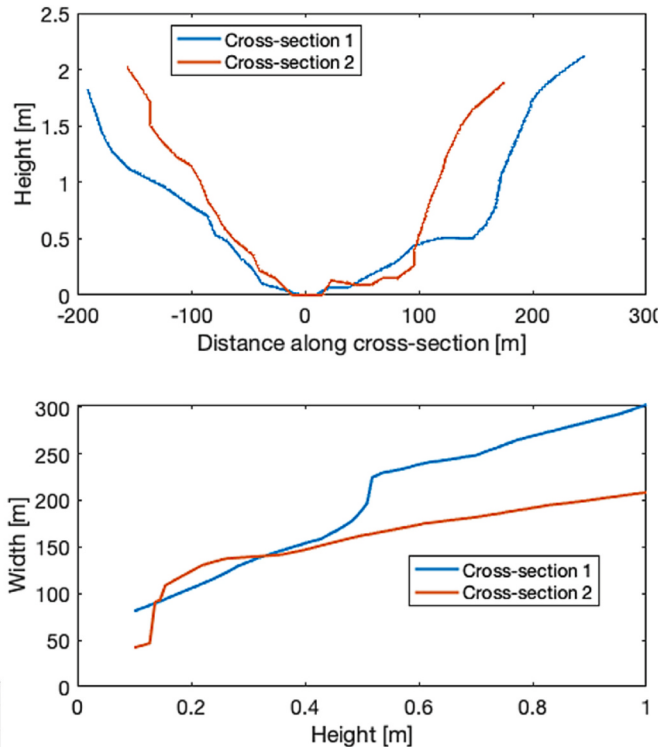
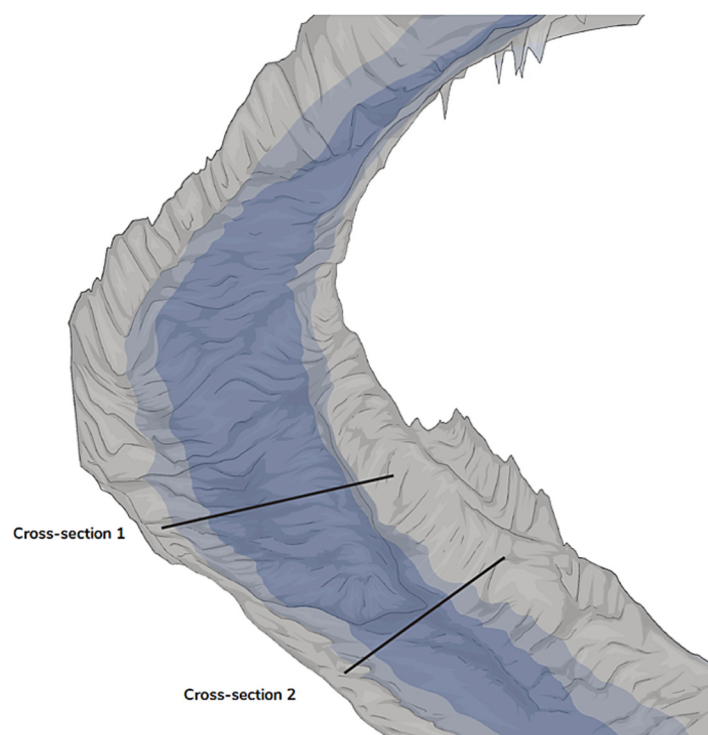


**Fig. 1.** Conceptual diagram illustrating fluvial hypsometry. The elevations of the river bed and surrounding topography in a) are a drawing based on an oblique view of bed topography of the Upper St Clair River (IUGLS, 2009). The different shades of blue and grey represent two different water surfaces superimposed on the riverbed topography. The blue and red lines in a) show two river cross-sections, which are shown as vertical elevations in b). The height-width relationships or river hypsometric curves for the two cross-sections are shown in c). (For interpretation of the references to colour in this figure legend, the reader is referred to the web version of this article.)

and  $e_t$  is the width residual for each index  $t$ : i.e., it is the difference between the true width, and the width predicted by the linear relationship as a function of WSE, as shown in Fig. 2 using an example, illustrative synthetically-generated dataset.

An important feature of river hypsometric curves is that integration of the function that predicts the relationship between width and WSE produces the cross-sectional area ( $A$ ):

$$A(H) = \int_{H_{\min}}^H W(H') dH' \quad (2)$$

where  $H'$  is a variable of integration, and  $H_{\min}$  is the WSE at which cross-sectional area is equal to zero, as shown by Coss et al. (2023).

In the next sections, we present an algorithm to compute river hypsometric curves from noisy measurements of WSE and width (section 2.1), present a method to compute estimates of WSE and width constrained to the river hypsometric curve (section 2.2), and show that river discharge estimated with the hypsometrically constrained WSE and width is more precise than that without hypsometric constraint by analytically computing the reduction in expected discharge error; we verify the discharge error reduction using a simple Monte Carlo experiment (section 2.3).

### 2.1. Estimating the river hypsometric curve from WSE and width measurements

The ordinary least squares fit chooses parameters  $p_0$  and  $p_1$  that minimize an objective function consisting solely of the sum of the squared width residuals, i.e., the vertical differences in Fig. 2:

$$\hat{p}_0, \hat{p}_1 = \underset{p_0, p_1}{\operatorname{argmin}} \sum_{t=1}^{n_t} e_t^2 \quad (3)$$

The “errors-in-variables” approach explicitly considers errors in both width and WSE, and thus considers both residuals in width ( $e_t$ ) and WSE ( $u_t$ ), thus modifying the objective function to be

$$\sum_{t=1}^{n_t} \frac{e_t^2}{\sigma_W^2} + \frac{u_t^2}{\sigma_H^2} \quad (4)$$

which is the so-called “statistical distance”, as defined by Fuller (his eq. 1.3.15), where  $\sigma_W^2$  and  $\sigma_H^2$  are the measurement error variances for both width and WSE, respectively. If the measurement error variances are

constant in time, Fuller shows (his eq. 1.3.20) that by substituting (1) into (4), the objective function can be rewritten as

$$\min_{p_0, p_1} \left[ (\sigma_W^2 - 2p_1\rho\sigma_H\sigma_W + p_1^2\sigma_H^2)^{-1} \sum_{t=1}^{n_t} (W_t - p_0 - p_1 H_t)^2 \right] \quad (5)$$

where  $\rho$  is the correlation between errors in the (unconstrained) width and WSE data.

Because river bed topography is the integrated, dynamic result of a number of geomorphic processes, including the physical work of water at both high and low flow, river hypsometric curves are often non-linear. Here, we follow the approach used in the SWOT data products (Stuurman et al., 2022) and use a piecewise-linear function to represent river hypsometry, with three sub-domains defined by WSE:

$$W(H) = \begin{cases} p_4 + p_5 H & H_1 \leq H \\ p_2 + p_3 H & H_0 \leq H < H_1 \\ p_0 + p_1 H & H < H_0 \end{cases} \quad (6)$$

where  $p_{i=0\dots 5}, i = 0, 1\dots 5$  are parameters defining the slope and intercept of the linear segments of the hypsometric curve between each sub-domain, and  $H_0$  and  $H_1$  are WSE breakpoints separating the sub-domains. We use three sub-domains to capture the frequently occurring phenomenon of a first sub-domain to capture the hypsometry within the channel when the water elevation is less than bank full, a second sub-domain to capture the hypsometry as width increases rapidly as flow goes out of bank, and a third sub-domain to capture hypsometry for out-of-bank flow. Other formulations could easily be considered as well, but we find the three sub-domains adequate for the data considered in this paper, as shown below. River hypsometric curves are mathematically continuous, and thus, we also require:

$$\begin{aligned} p_0 + p_1 H_0 &= p_2 + p_3 H_0 \\ p_2 + p_3 H_1 &= p_4 + p_5 H_1 \end{aligned} \quad (7)$$

In principle, the eight parameters defined in eq. (5) above could all be estimated simultaneously via a non-linear optimization algorithm. However, we have found it is far more computationally efficient to make an approximation and first choose the breakpoints  $H_0$  and  $H_1$  based on an ordinary least squares approach, and then compute optimal parameters  $p_i, i = 0, 1\dots 5$  based on the errors-in-variable cost functions (Eq. 5), using the WSE breakpoints as estimated by ordinary least squares. In other words, the first step fits a three-part piecewise linear function to the data using OLS, selecting both the breakpoints and the fit

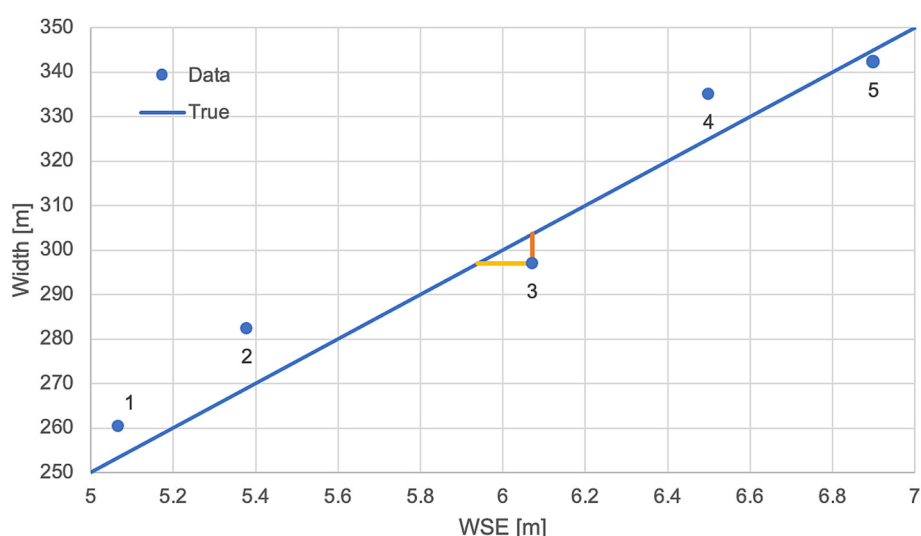


**Fig. 2.** Example data illustrating width and WSE relationships and defining residual quantities. Data labels indicate data index,  $t = 1, 2, \dots, 5$ . The true relationship for this illustrative case is  $W = 50H$ , and is shown using the blue line. The “Data” were generated randomly using  $\sigma_W=10$  m,  $\sigma_H=0.10$  m. The red and orange lines illustrate the fit residuals for width and WSE, respectively; the red and orange lines for  $t = 3$  illustrate  $e_t$  and  $u_t$ , respectively.

parameters. Then the second step chooses the fit parameters using the breakpoints chosen in the first step, and the EIV approach. These algorithms are all implemented in a publicly available software package described in the Acknowledgments. The optimization algorithm is a steepest-descent type algorithm, and more specifically uses a “trust-constraint” approach. The software automatically differentiates the objective function and constraints. Users are referred to the software package for further details.

## 2.2. Constraining WSE and width measurements to a river hypsometric curve

In this section, we use the hypsometric curve computed as described in the previous section to create new estimates of both WSE and width, constrained to the hypsometric curve. Furthermore, we show that these hypsometrically constrained WSE and width measurements improve discharge precision. From Fuller's eq. 1.3.17, an estimate of the true WSE values ( $\hat{H}_t$ ) is given by:

$$\hat{H}_t = H_t - \frac{\hat{s}_{uv}}{\hat{s}_{vv}} \hat{v}_t \quad (8)$$

where:

$$\hat{v}_t = W_t - \hat{p}_j - \hat{p}_k H_t$$

$$\hat{s}_{uv} = \rho \sigma_H \sigma_W - \hat{p}_k \sigma_H^2$$

$$\hat{s}_{vv} = \sigma_W^2 - 2\hat{p}_k \rho \sigma_H \sigma_W + \hat{p}_k^2 \sigma_H^2$$

and where  $j$  and  $k$  subscripts refer to the appropriate parameters for intercept and slope, respectively, for the sub-domain that a data point falls into. In this paper, we assume  $\rho = 0$ , because no information on this correlation is currently available. Such information could become available in the future, e.g. after analysis of SWOT WSE and width errors. The domain assignment is done by computing  $\hat{H}$  of a given observation for each of the three sub-domains, and then choosing the subdomain for which  $\hat{H}$  is within the subdomain WSE bounds.

The uncertainty in the constrained WSE as estimated via eq. (8) is given by Fuller's eq. 1.2.28:

$$\sigma_H^2 = \sigma_H^2 - \frac{\hat{s}_{uv}^2}{\hat{s}_{vv}} \quad (9)$$

A crude estimate of the width error uncertainty, which has proved robust in offline experiments (not shown) over the ranges of data uncertainties in this paper can be given by:

$$\sigma_W^2 = \hat{p}_k^2 \sigma_H^2 \quad (10)$$

The constraint changes the uncertainties and imposes a correlation on the new estimates of width and WSE (analyzed in the following subsection), but note that the constrained WSE and width are still random variables.

## 2.3. Exploring effects of hypsometric constraints on remote sensing of discharge

This section explores whether the discharge uncertainty is expected to increase or decrease, given the WSE and width uncertainty and corresponding error correlation resulting from the hypsometric constraint. Assume the new height and width error standard deviations are given by  $\sigma_{Hc}$  and  $\sigma_{Wc}$ , respectively, and then define the fractional reductions in the error standard deviations for WSE and width to be  $f_{HR}$  and  $f_{WR}$ , respectively, as given by

$$\sigma_{Hc} = (1 - f_{HR}) \sigma_H \quad (11)$$

$$\sigma_{Wc} = (1 - f_{WR}) \sigma_W \quad (12)$$

The correlation coefficient between the height and width errors after applying the hypsometric constraint is given by  $\rho_{HW}$ .

Assume a simple flow law predicting river discharge  $Q$  from measured river properties and unmeasured parameters, given by:

$$Q = \frac{1}{n} (H - H_0)^{5/3} WS^{1/2} \quad (13)$$

where  $S$  is river slope, and  $n$  and  $H_0$  are calibration coefficients or flow law parameters nominally defined as resistance coefficient and river bottom elevation, respectively. The error variance associated with height and width error for the hypsometrically unconstrained discharge is then given by:

$$\left( \frac{\sigma_Q}{Q} \right)^2 = \overline{\left( \frac{5}{3} \frac{\sigma_H}{H_t - H_0} \right)^2} + \overline{\left( \frac{\sigma_W}{W_t} \right)^2} \quad (14)$$

where the overline indicates a temporal average. This expression contains only uncertainty due to height and width because our intent is to describe how the height-width constraint impacts discharge uncertainty, and the remaining variables ( $n, H_0, S$ ) are not impacted by the constraint. The expression for the constrained case is similar, but with an additional term representing the correlation of errors between the constrained WSE and width estimates:

$$\left( \frac{\sigma_Q}{Q} \right)_c^2 = \overline{\left( \frac{5}{3} \frac{\sigma_{Hc}}{H_t - H_0} \right)^2} + \overline{\left( \frac{\sigma_{Wc}}{W_t} \right)^2} + \sigma_{Wc} \sigma_{Hc} \rho_{HW} \frac{10}{3} \frac{1}{W_t(H_t - H_0)} \quad (15)$$

We assess whether or not discharge estimates are improved or degraded via the hypsometric constraint by defining the reduction in variance ( $\delta$ ), which is equal to the difference in error variance for the hypsometrically constrained and unconstrained discharge ( $Q$  and  $Q_c$ ), and the true is  $Q_*$ .

The actual relative error variance is:

$$\left( \frac{\sigma_Q}{Q} \right)^2 = \text{Var} \left[ \frac{Q - Q_*}{Q_*} \right]$$

where  $Q_*$  is the true discharge. Then the reduction in variance is:

$$\delta = \left( \frac{\sigma_Q}{Q} \right)^2 - \left( \frac{\sigma_Q}{Q} \right)_c^2 \quad (16)$$

Combining eqs. 14–16, we have this expression for the estimated reduction in discharge error variance as a function of the height and width error:

$$\begin{aligned} \delta = & \left[ 1 - (1 - f_{HR})^2 \right] \sigma_H^2 \overline{\left( \frac{5}{3} \frac{1}{H_t - H_0} \right)^2} \\ & + \left[ 1 - (1 - f_{WR})^2 \right] \sigma_W^2 \overline{\left( \frac{1}{W_t} \right)^2} \\ & - (1 - f_{HR})(1 - f_{WR}) \sigma_W \sigma_H \rho_{HW} \frac{10}{3} \frac{1}{W_t(H_t - H_0)} \end{aligned} \quad (17)$$

From this equation, discharge variance must decrease as a result of hypsometrically constraining height and width, under the expected conditions that  $f_{HR} \geq 0$ ,  $f_{WR} \geq 0$ ,  $\rho_{HW} \geq 0$ . The infrequent cases with  $f_{HR} < 0$  or  $f_{WR} < 0$  are discussed in the following paragraph.

To explore this further, we present a “toy” problem with a sinusoidal WSE timeseries with amplitude of 1.0 m, an offset of 200 m, a corresponding width timeseries assuming that width increases 30 m for every one meter of WSE increase. Further parameters are specified to be  $n = 0.03$  and  $S = 30 \text{ cm/km}$ ,  $H_0 = 198 \text{ m}$ , and discharge is computed using the flow law above. WSE and width errors were added with error standard deviations specified over a wide range. Fig. 3 shows the height and

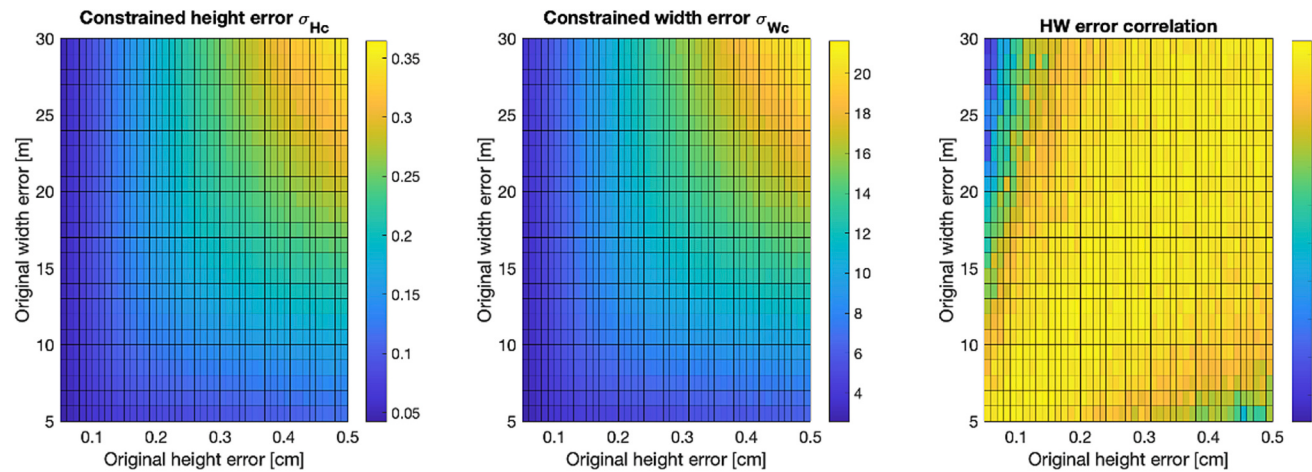


**Fig. 3.** Example results of constraining height and width with the “toy” river problem described in the text. Units are meters for both height and width in the left and center figure. Correlation (in right figure) is dimensionless.

width error standard deviations after constraint, and the resulting correlation in height and width error, all computed across the timeseries.

Fig. 4 shows the reduction in height, width and discharge error as a

result of applying the hypsometric constraint. For example, when original height error is  $\sim 40$  cm, and original width error is  $\sim 5$  m, then the height error is reduced significantly (this is similar to the precision of

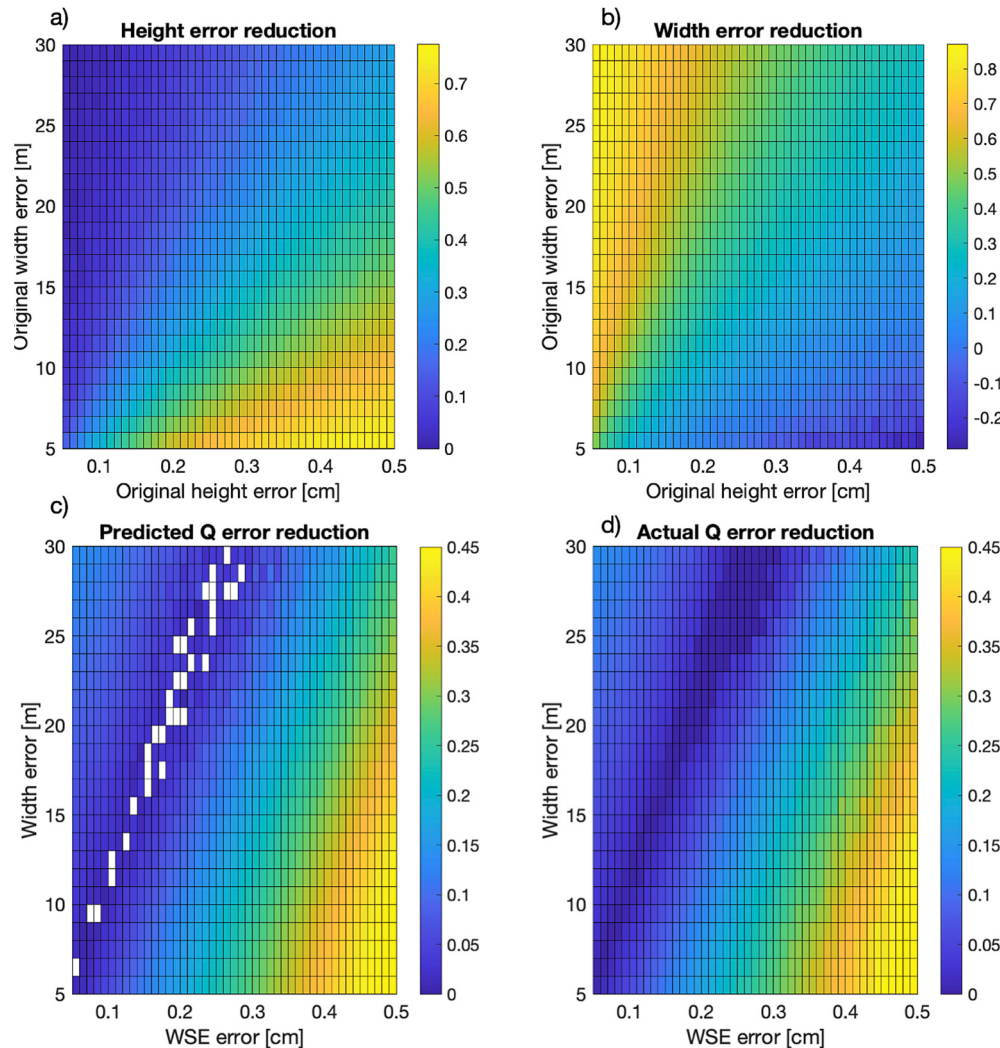


**Fig. 4.** Example impact of constraining height and width on river discharge accuracy in simple toy experiment. The top two figures show fractional reduction in height and width error standard deviation  $f_{HR}$  and  $f_{WR}$  respectively. The bottom two figures show predicted (left) and actual (right) reduction in discharge error standard deviation. For results of the Monte Carlo experiment in c, a small number of Monte Carlo experiment result in a divide-by-zero, shown as white.

height and width data estimated from the commercial imagery presented below). Similarly, when width error is 25 m, and height error is 10 cm, then the width error becomes significantly more precise (this is similar to the expected SWOT accuracy). Note that some degradations in WSE and width error can occur in a narrow range when width error is relatively precise and WSE error is relatively imprecise. The predicted discharge error reduction from eq. 17 based on WSE and width error is shown in Fig. 4c, and the actual discharge error reduction based on the realizations of discharge timeseries in the Monte Carlo experiment is shown in Fig. 4d. Both Fig. 4 c and d demonstrate that discharge uncertainty is expected to be reduced, despite the height and width error correlation, and occasional decrease in the precision of one quantity or the other. We have demonstrated that constraining height and width improves discharge precision for a simple flow law using this toy problem experiment. Later in the paper, we will next demonstrate that it also improves discharge error estimates using more complex flow laws and real data.

In summary, constraining measurements to fall on a river hypsometric curve changes the stochastic properties of WSE and width. The uncertainties in constrained WSE and width largely decrease, and the constrained WSE and width errors are correlated. However, the net effect is to reduce the uncertainty in river discharge predictions from remote sensing, at least for the toy case presented, across a wide range of expected river discharge uncertainty. The rest of this study explores whether or not this improvement in discharge accuracy is borne out using real remote sensing data.

### 3. Study area and datasets

We assess flow law accuracy using *in situ* stage and discharge measurements at five stream gages throughout Alaska and Canada (Table 1). These five stream gages have more than 10 usable high-resolution images and accompanying digital elevation models (DEMs) available that overlap with gaged records; none of the other 215 gages in United States and Canada (see section 3.1 and section 3.12 for imagery and gage details) examined meet this criterion. We select reaches to maximize the number of discrete observations and observed reach length. Note that spatial coverage varies from one image to the next over the same gage. We sum the total number of images that cover each point posted every 30 m along the SWORD database (see section 3.3) centerline at each gage, and manually select reach bounds that lead to the largest number of fully observed points along each river. Because imagery spans an exceptionally long portion of the river at Tanana near Fairbanks, we split that site into two reaches (see section 4.3), for a total of six reaches in all. The river reaches and gage locations along with their geographic locations are shown in Fig. 5. The Liard, Meade, and Tanana at Nenana are all single channel reaches. The other three reaches have multiple channels. The Tanana at Fairbanks Downstream includes several channels in the upstream part of the reach (bottom part of Fig. 5e), which merge into a single channel towards the downstream end of the reach. The Sagavanirktok reach generally has 2–3 channels; note that the

**Table 1**

Stream gages used in this study from Environment and Climate Change Canada (Liard) and the United States Geologic Survey (remaining). Mean flow is computed across all available instantaneous discharge measurements over the past twenty years.

River name	Gage Id	Latitude [°]	Longitude [°]	Mean Flow [m <sup>3</sup> /s]
Liard River	10AA001	60.051	-128.907	438.3
Meade River	15803000	70.495	-157.396	42.1
Sagavanirktok River	15908000	69.016	-148.818	129.9
Tanana River at Fairbanks	15485500	64.792	-147.841	1045
Tanana River at Nenana	15515500	64.565	-149.094	1276

image shown in Fig. 5c is at high flow, and more channels are visible in low flow images (not shown). The Tanana Fairbanks Upstream reach is far more complex, with a large number of channels.

#### 3.1. Imagery and DEMs

We use multispectral imagery as well as panchromatic imagery from Quickbird2, WorldView1, WorldView2, WorldView3, and GeoEye. The images were the basis of creating classified water masks and were also used to create ArcticDEM digital elevation models.

We use 2 m resolution digital elevation models provided by the ArcticDEM project as the basis for retrieving river surface heights. ArcticDEM is a large collection of Digital Elevation Models (DEMs) covering all land areas above 60 degrees north latitude and all of Greenland, Alaska, and Kamchatka (Porter et al., 2022). Created from stereophotogrammetry applied to commercial satellite imagery, the accuracy of these DEMs can be decimetric. ArcticDEMs are produced and openly distributed by the Polar Geospatial Center (PGC) (<https://www.pgc.umn.edu/data/arcticdem>, last accessed August 1, 2023). Based on stereophotogrammetry using the Surface Extraction from TIN-based Search-space Minimization (SETSM) software (Noh and Howat, 2015, 2017), ArcticDEM provides maps of first surface, not necessarily ground, elevation because neither vegetation nor manmade structures are removed. Typical coverage of a single DEM is about 17 km in width and 110 km in length. An example DEM is shown in Fig. 6. Multiple DEMs are available from ArcticDEM for each area we analyze; we choose the DEM produced at lowest water elevation in order to maximize its use in overlaying inundated imagery on the elevation model, as described below.

#### 3.2. Gage data

We use river stage and discharge data at 15 min temporal resolution obtained from USGS Instantaneous Values Web Service (<https://nwis.waterservices.usgs.gov/>) and from Environment and Climate Change Canada (<https://wateroffice.ec.gc.ca/>) for the five gages shown in Table 1. Discharge data values are matched to remote sensing imagery if the difference in timestamps is one day or less.

#### 3.3. SWORD

We use the SWOT a priori river database (SWORD) river centerlines (Altenau et al., 2021) to define reaches (Fig. 5). SWORD was built to support the SWOT mission and includes centerlines for rivers globally. Using a globally available dataset expands the potential reach of the methods described here.

### 4. Methods

#### 4.1. Image selection

We use a combination of automatic and manual filtering to identify images that were contaminated by river ice, clouds, or cloud shadows, or were otherwise of poor quality. River ice impacts water classification and width estimation and *in situ* discharge accuracy, as well as the theoretical applicability of the flow laws.

#### 4.2. Image classification

To obtain river masks from which to extract shoreline widths, we developed novel deep learning tools. Details are presented in a separate paper (Moortgat et al., 2022), in which we analyze five different state-of-the-art fully convolutional networks (FCN) based on the U-Net family (U-Net and the more efficient LinkNet, each with both ResNet-18 and ResNet-34 backbones, as well as the water-specific DeepWaterMap network). Each model was adapted to accommodate four optical bands

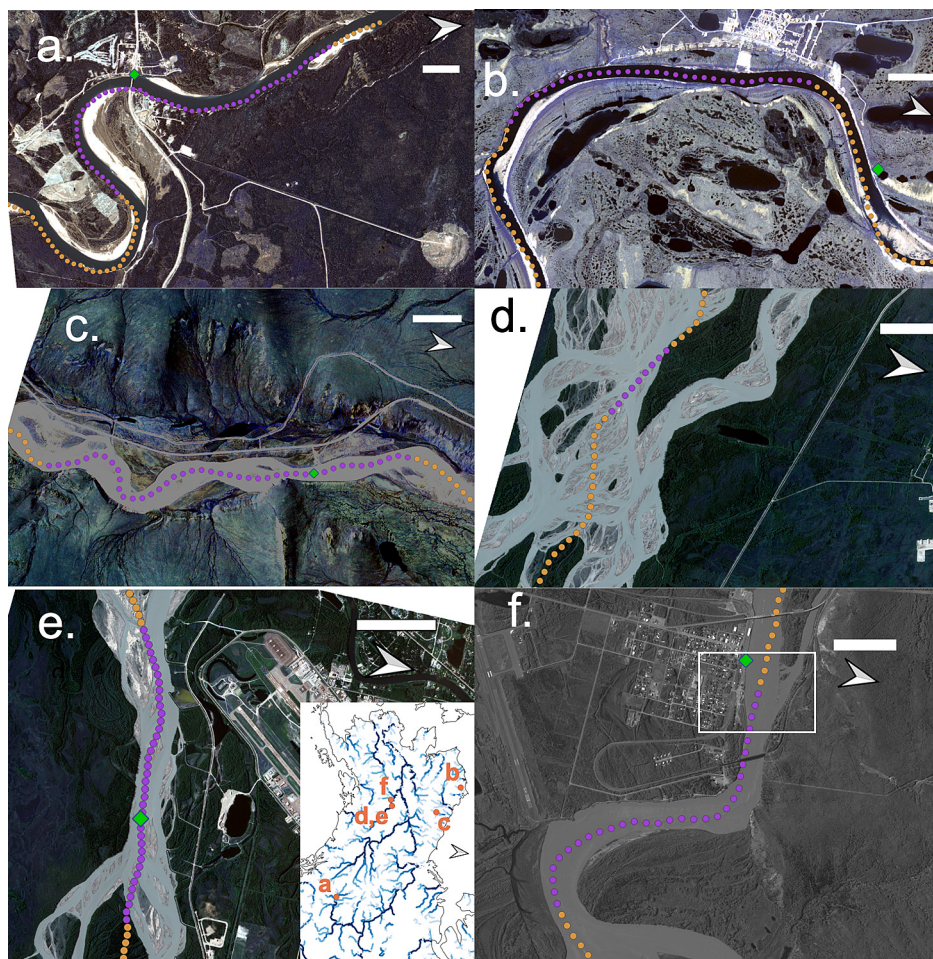


**Fig. 5.** Imagery showing river planform for the Liard (a), the Meade (b), the Sagavanirktok (c), the Tanana at Fairbanks Upstream (d), the Tanana at Fairbanks Downstream (e), and the Tanana at Nenana (f); all maps are in the polar stereographic projection, following ArcticDEM convention. Green diamonds show gage locations, and purple points represent the nominal river reach centerline; orange points represent centerline datapoints not selected for inclusion in study reach (shown for context). Locations of each image can be identified using the inset map or the gage locations provided in Table 1. Note that the gage location for the Tanana at Fairbanks gage falls within the downstream, but not the upstream figure. The filled white rectangle on the right side of each image spans a distance of 500 m. All images shown are multispectral, except for f, which is panchromatic. The map inset in panel e shows the location of each river reach, along with coastlines and a map of SWORD rivers where darker blue indicates larger drainage area. The white outline in panel f indicates the spatial extent of a map presented below in Fig. 7. Imagery © 2021, MAXAR, Inc. (For interpretation of the references to colour in this figure legend, the reader is referred to the web version of this article.)

(RGB-NIR) and enhanced with image augmentation techniques tailored to satellite imagery (Isikdogan et al., 2020). We found that for multispectral imagery, DeepWaterMap provides the optimal river classification in terms of speed, memory requirements, and accuracy: all models achieved >90 % F1 scores on validation data (Moortgat et al., 2022).

In a novel approach, we then used (post-processed) river masks generated from multispectral imagery as training data for the same five segmentation models, but now trained on synchronous panchromatic images. Impressively, the U-Net and LinkNet models (with both ResNet-18 and ResNet-34 backbones) still achieved  $\geq 85\%$  accuracy (F1 scores) on validation data. Unlike pixel-level classifiers, fully convolutional neural networks (FCN) consider not only the spectral information of individual pixels but also larger-scale morphologies (edges, gradients, etc.), which allows these deep learning models to accurately detect river ‘shapes’ even from panchromatic images. This ability was critical for this work because roughly twice as many panchromatic images are available from these commercial satellites versus multispectral images. As mentioned above, even with both multispectral and panchromatic imagery, only a small number of gages have sufficient repeat coverage to allow statistically significant analyses of hypsometry and river flow laws. Note that the panchromatic images have  $\sim 4 \times$  higher spatial resolution. In this work, we chose to perform all analyses at the  $\sim 1.5\text{-m}$

native spatial resolution of the multispectral imagery, using DeepWaterMap for multispectral and U-Net with ResNet-18 for panchromatic images.

#### 4.3. Long profile estimates of width and height

We estimate river width and height at 100 m spatial posting along river centerlines (referred to as “long profiles” hereafter) using the “imagery-altimetry” method described by Dai et al. (2018): Classified images are intersected with low-stage DEMs, and the resulting shoreline elevations are mapped onto the river centerlines from SWORD. We additionally use “direct method” elevations where available, as described by Dai et al. (2018), but this is a small part of the data used, as only a small fraction of the available images are stereographic pairs. Dai et al. (2018) found that the direct method and the image-altimetry method produce consistent results with comparable error statistics.

Following Dai et al. (2018), we compute the WSE at each node along the river centerline, where nodes are centerline locations posted at 100 m intervals along the river. The WSE and width of each node for each satellite pass is defined as the 25th percentile of all pixels associated with the node to filter out high elevation outliers. The choice of the 25th percentile was made via sensitivity studies performed by Dai et al.

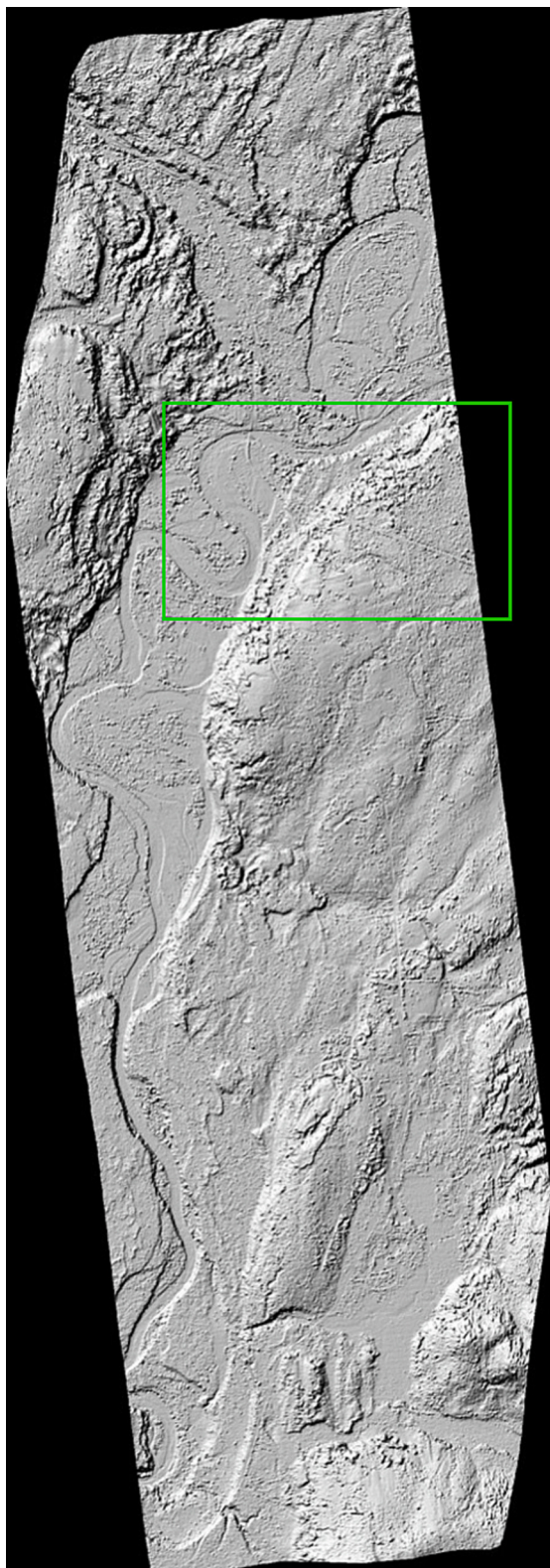


**Fig. 6.** Example hillshade of a 2-m digital elevation model of the Liard River. The green rectangle denotes the same spatial extent as Fig. 5a; for scale, the long dimension of the green rectangle is approximately 5.5 km. The map is shown in polar stereographic projection. Image location can be identified using the gage location for the Liard River gage provided in Table 1. Created from MAXAR, Inc. imagery. (For interpretation of the references to colour in this figure legend, the reader is referred to the web version of this article.)

(2018), looking at a single river (the Tanana near Fairbanks). No elevation is estimated for any node that has fewer than 20 pixels, or a pixel standard deviation greater than 250 cm. We refine node WSE estimates by fitting a monotonic decreasing surface to the node elevations of the long profile, removing any pixels falling further than 100 cm from the fitted surface, and recomputing node WSE elevations. We estimate river width at each node using the RivMap toolbox (Schwenk et al., 2017). The average width is computed at each node, based on taking the total inundated area and dividing by the distance between nodes. Example long profiles of width and WSE for the Sagavanirktok River are shown in Fig. 8; profiles on the remaining rivers are shown in Figure S-1.

#### 4.4. Reach averaging

We select reaches as described above in the text at beginning of section 3, before the beginning of section 3.1. Reach averaged WSE is computed in a way that is robust to partial reach observation. If reach averaged WSE were computed as the simple average of the WSE measurements at each node, partial reach observation would lead to a bias in WSE. For example, if the upstream part of a fairly steep reach is not observed, the resulting average could be significantly biased too low by tens of cm. We use a simple correction to avoid bias:

$$H = \langle H_{node} \rangle + \frac{1}{2} S(s_1 + s_2) \quad (18)$$

where  $H$  is the reach averaged WSE after applying the slope correction,  $\langle H_{node} \rangle$  is the average of the observed WSE values at each node,  $S$  is the reach slope, and  $s_1$  and  $s_2$  denote the flow distance of the boundaries of the observed part of the reach. The  $s$  values are defined for each node to increase from upstream to downstream, and to be zero at the reach center point. Thus, in the case of a fully observed reach,  $H = \langle H_{node} \rangle$ , as expected. This approach can correct for the systematic effects of partial reach observation, but we specify that the reach must be at least 80 % observed, to avoid large random errors in the reach averaged WSE measurements.

The reach averaged width is computed as the simple average of the node width measurements. Note that reach averaged river width is far less sensitive to partial observation, as river WSE changes dramatically downstream as a function of its slope. For example, visual inspection indicates that missing 500 m of the width nodes on the Sagavanirktok River (see Fig. 8, bottom) would not introduce a large bias.

Reach averaged river slope is measured for each long profile by computing a linear relationship minimizing the least squares of the WSE fit residuals. Reach slope is treated as a constant in time for all analyses. Altenau et al. (2019) measured low temporal variability in slope on the Tanana River between the Tanana River at Fairbanks Downstream and the Tanana River at Nenana reaches, so it is possible that slope does not vary significantly for many of the reaches in this study. Constant river slope is estimated as the median slope across the observed profiles, rounded to the nearest 5 cm/km (Table 2). Note that in all flow laws (section 4.5), the square root of slope is a multiplicative term, and that there is a multiplicative calibration parameter; thus, when slope is treated as a constant, then slope inaccuracy may lead to unrealistic values of flow law calibration parameters, but will have less impact on flow law performance metrics.

#### 4.5. Flow laws

We evaluate seven flow laws relating WSE, river width, and slope to river discharge. Each of these flow laws expresses river discharge as a function of two types of variables: observations and flow law parameters. The observations are WSE, width, and slope, along with one derived quantity, the change in cross-sectional area, that is computed as the integral of the hypsometric curve as described in Section 2.1. Note that the change in cross-sectional area can be computed with regard to any

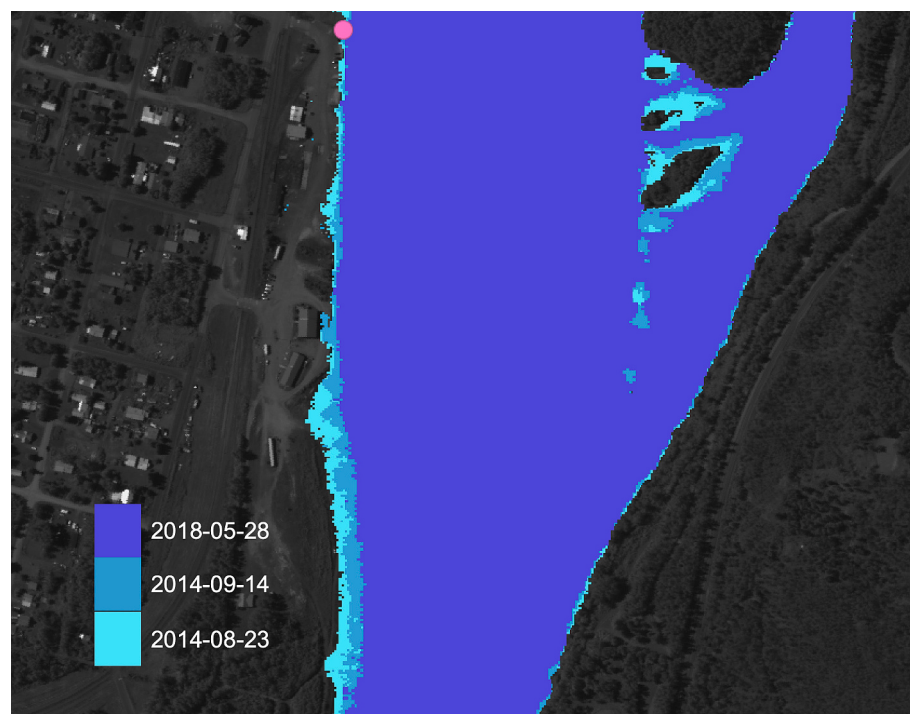


**Fig. 7.** Three water segmentation masks, collected on different dates, overlaid on imagery are shown as three different shades of blue, for the Tanana River at Nenana. The gage location is shown as a pink circle. Image location can be identified using the Tanana River at Nenana gage location provided in Table 1. The stage on the three dates is 2.16 m, 1.76 m, and 2.42 m, respectively. The background image is the same panchromatic image shown in Fig. 5f. The extent of this image is indicated by a white outlined rectangle in Fig. 5f and is 750 m in the vertical direction. Imagery © 2021, MAXAR, Inc. (For interpretation of the references to colour in this figure legend, the reader is referred to the web version of this article.)

constant; here we select the first measurement in the timeseries. The flow law parameters are the remaining time-invariant terms that appear in the flow law, including quantities such as river bed elevation, parameters governing resistance to flow, and other variables that lack physical meaning such as power law coefficients and exponents. In this study, all flow law parameters are computed via calibration to true discharge as measured at the gaging stations in an attempt to isolate the effect of the flow law error itself.

At-a-station hydraulic geometry (AHG) is a concept first introduced by Leopold and Maddock (1953) and relates river width, depth, and velocity to discharge. We evaluate two AHG relationships:

$$Q_t = aW_t^b \quad (19)$$

is the AHG relationship for river width, where  $a$  and  $b$  are the AHG coefficient and exponent, respectively, and are the flow law parameters to be calibrated. The “ $t$ ” subscripts in this and later equations denote that a quantity is time-varying. The AHG relationship for river depth is

$$Q_t = c(H_t - H_0)^d \quad (20)$$

where  $c$  and  $d$  are the AHG coefficient and exponent, respectively. Depth is approximated by the difference between measured water surface elevation ( $H_t$ ), and an offset  $H_0$  which is the river bed elevation. The flow law parameters to be calibrated are thus  $c$ ,  $d$ , and  $H_0$ . Note that this is also identical to the so-called “rating curve” relationships typically used to relate river discharge to measured stage for in situ streamflow monitoring.

The Gauckler-Manning-Strickler equation relates frictional losses to the  $2/3$  power of the hydraulic radius (i.e., the river cross-sectional area divided by the wetted perimeter) and to the square of the average river velocity. The Gauckler-Manning-Strickler relation is typically considered to be a uniform flow law, unsuited to application in natural channels with significant spatial variability. However, as described by Frasson et al. (2021) and Tuozzolo et al. (2019), use of the surface slope

for  $S$  makes this equation more analogous to a diffusive wave approximation under gradually varied flow assumptions rather than a uniform flow equation. We refer to this as the “modified Manning’s equation”.

We examine several forms of the modified Manning’s equation. The simplest form equates hydraulic radius to river depth:

$$Q_t = \frac{1}{n}(H_t - H_0)^{5/3} W_t S^{1/2} \quad (21)$$

where  $n$  is Manning’s coefficient, which represents energy losses due to friction, and  $S$  is the river surface slope. In this equation,  $n$  and  $H_0$  are flow law parameters estimated by calibration. This equation invokes the so-called “wide river” approximation, implicitly assuming that river depth is much less than river width, which is a safe assumption for the large rivers considered in this study. This form of Manning’s equation will be referred to as “Manning’s equation for height” hereafter.

In a slightly more general form, Manning’s equation can represent hydraulic radius as cross-sectional area divided by river width, still invoking the wide-river approximation, but making no assumption regarding river shape:

$$Q_t = \frac{1}{n}(A_0 + \delta A_t)^{5/3} W_t^{-2/3} S^{1/2} \quad (22)$$

where  $A_0$  and  $\delta A_t$  are the cross-sectional area at the initial time series point, and the change in cross-sectional area for subsequent times. In this equation,  $n$  and  $A_0$  are flow law parameters estimated by calibration. This form is referred to as “Manning’s equation for area with constant  $n$ ”, hereafter.

Due to spatial variability within a reach,  $n$  has been found to vary strongly in time in the modified Manning’s equation (Durand et al., 2016; Rodriguez et al., 2020). Several adaptations have been considered for  $n$ , including a power law as a function of hydraulic depth (the ratio of cross-sectional area to width):

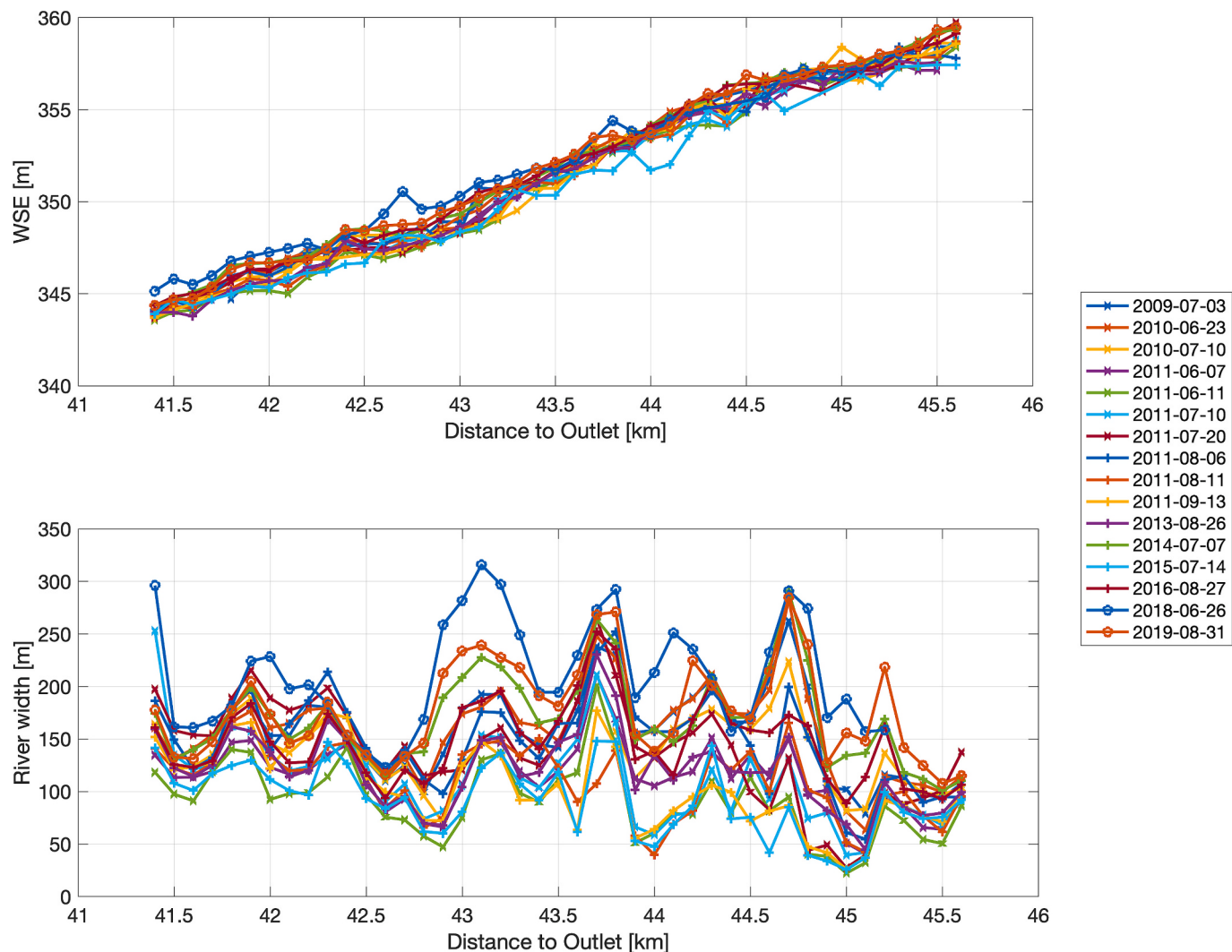


**Fig. 8.** Example long profiles for the Sagavanirkok River. A total of 17 profiles are shown.

**Table 2**

Basic properties of selected river reaches. The number of channels was counted manually from the imagery. Average width is computed over all overpasses and all river nodes.

River name	Number of channels	Average width [m]	Reach length [km]	Slope [cm/km]
Liard River	1	195.4	5.5	50
Meade River	1	151.9	3.5	10
Sagavanirkok River	2–3	137.6	3.4	370
Tanana River at Fairbanks - Upstream	4–6	738.6	1.0	45
Tanana River at Fairbanks - Downstream	1–4	445.3	4.0	45
Tanana River at Nenana	1	284.0	3.1	20

$$Q_t = \frac{1}{n_t} (A_0 + \delta A_t)^{5/3} W_t^{-2/3} S^{1/2} \quad (23a)$$

$$n_t = n_0 \left( \frac{A_0 + \delta A_t}{W_t} \right)^p \quad (23b)$$

In this scheme,  $n_0$ ,  $p$  and  $A_0$  are flow law parameters estimated by

calibration. This flow law is referred to as “Manning’s equation for area with power law  $n$ ” hereafter.

A more physical basis for  $n_t$  has been derived by Rodriguez et al. (2020), who showed that spatial variations in the parameters of the modified Manning’s equation create temporal variations in  $n_t$ . Changes in depth are more important than width, based on the differing exponents. Considering only the variations in depth, and making an approximation of a constant surface slope within the reach, leads to the following formulation:

$$n_t = n_\infty \left( 1 + \frac{5}{6} \left[ \frac{\sigma_Z W_t}{A_0 + \delta A_t} \right]^2 \right) \quad (24)$$

where  $n_\infty$  is the friction coefficient at high flow where spatial variations in parameters tend to have minimal effect, and  $\sigma_Z$  is the spatial standard deviation in river bed elevation. In this approach, flow is computed by combining Eqs. 24 and 23a. The flow law parameters estimated by calibration are  $n_\infty$ ,  $\sigma_Z$ , and  $A_0$ .

The final flow law to be evaluated is the Modified Optimized Manning Method Algorithm (MOMMA) algorithm similar to that derived by Bjerkli et al. (2018), as presented by Frasson et al. (2021):

$$n_t = n_b \left( 1 + \log \left[ \frac{H_b - B}{H_t - B} \right] \right) \quad (25a)$$

$$Q_t = \frac{1}{n_t} \left( [H_t - B] \frac{r}{1+r} \right)^{5/3} W_t S^{1/2} \quad (25b)$$

where  $n_b$  is the bankfull friction coefficient,  $H_b$  is the bankfull WSE,  $B$  is the river bed elevation, and  $r$  is a river shape parameter. All flow law parameters are estimated by calibration using a steepest-descent solver to minimize the squared difference of the flow law prediction and observed discharge, across the timeseries. This flow law parameter estimation is performed using the software package referenced in the Acknowledgments. In this study, we focus on the accuracy of the flow laws themselves, so we calibrate them using field data, rather than using mass-conserved flow law inversion methods to estimate flow law parameters as described by Frasson et al. (2021).

#### 4.6. Flow law evaluation

We use all datapoints in both calibration and validation. We match remotely sensed data to gage data if the difference in timestamp is less than one day. We evaluate each flow law accuracy using three metrics. As we are calibrating to field data, there will be minimal bias in the discharge predictions as evaluated against the gage data. Normalized RMSE (nRMSE) is the root mean squared error, normalized by the true mean flow:

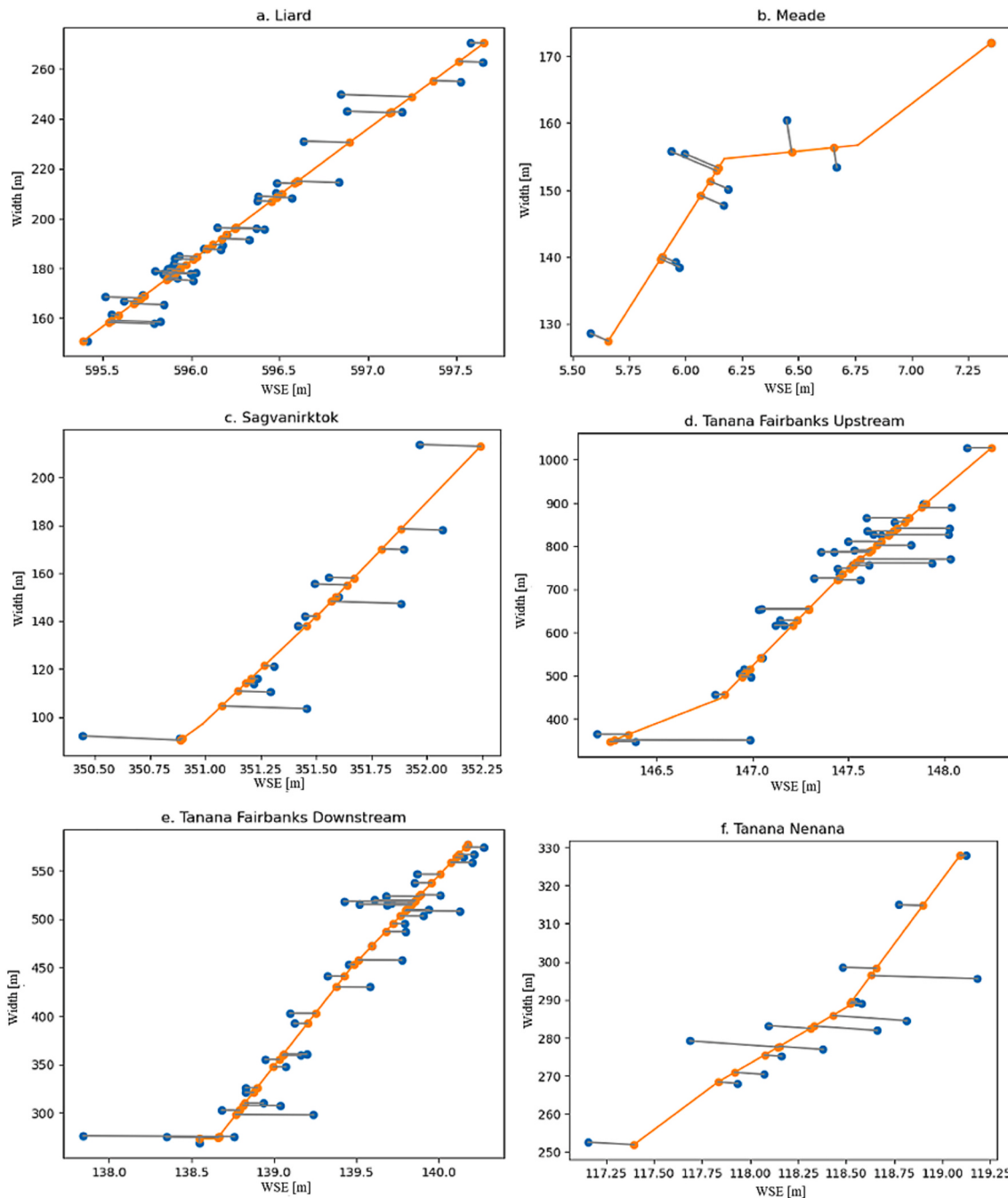


**Fig. 9.** River hypsometric curves for all six reaches (orange lines), along with the unconstrained (blue) and the constrained (orange) observations of WSE and width. The constrained and unconstrained datapoints are connected with grey lines, to illustrate the effect of the hypsometric constraint. (For interpretation of the references to colour in this figure legend, the reader is referred to the web version of this article.)

$$nRMSE = \frac{\sqrt{\frac{1}{n} \sum_{t=1}^n (\hat{Q}_t - Q_t^*)^2}}{\frac{1}{n} \sum_{t=1}^n Q_t^*} \quad (26)$$

where  $\hat{Q}_t$  is the estimate of discharge from a flow law combined with remote sensing data at time  $t$ , and  $Q_t^*$  is the true discharge at time  $t$ . The nRMSE is zero for a perfect estimate. The normalized Mean Absolute Error (nMAE) is similar to nRMSE but is computed on the absolute value of the errors, rather than on the square of the errors:

$$nMAE = \frac{\frac{1}{n} \sum_{t=1}^n |\hat{Q}_t - Q_t^*|}{\frac{1}{n} \sum_{t=1}^n Q_t^*} \quad (27)$$

The nMAE is generally less sensitive to outliers than is the nRMSE. The Kling-Gupta Efficiency (KGE) combines several metrics of performance:

$$KGE = 1 - \sqrt{(\rho_{KGE} - 1)^2 + (\beta - 1)^2 + (\gamma - 1)^2} \quad (28)$$

where  $\rho_{KGE}$  is the correlation coefficient,  $\beta$  is the ratio of the time average estimated flow to the time average true flow ( $\hat{\bar{Q}}$ ),  $\beta = \frac{\hat{\bar{Q}}}{\bar{Q}}$ , and  $\gamma$  is the ratio of the coefficient of variation of the estimated to true flow  $\gamma = \frac{\sigma_{\hat{Q}}}{\bar{Q}} \frac{\bar{Q}^*}{\sigma_{Q^*}}$ , where  $\sigma_{\hat{Q}}$  and  $\sigma_{Q^*}$  are the time series standard deviation of the estimated and true flow respectively.

## 5. Results and discussion

### 5.1. River hypsometry

The river hypsometry of the six river reaches is shown in Fig. 9. The slopes of these hypsometric curves, summarized in Table 3, vary by over an order of magnitude from a minimum of 26.3 m width/m stage on the Meade River to a maximum of 341 m/m on the Tanana River at the Fairbanks upstream reach. These findings highlight that significant changes in river hypsometric slopes occur between reaches that are kilometers in length, ranging from tens to hundreds of meters width increase per meter of WSE increase.

The river hypsometric curve within each reach shows significant variability in some, but not all, river reaches. For example, the hypsometry of the Tanana River at Fairbanks Upstream reach shows a gentle slope (173 m/m) at lowest WSE values, followed by a steep section (450 m/m), and then a more modest slope (375.9 m/m). One way to measure

**Table 3**

River hypsometry characteristics. The average hypsometric slope is computed as the range of the widths divided by range of WSE data constrained to the hypsometric curve.

River Name	Average river hypsometric slope [m/m]	Within-reach hypsometric slope variability	Hypsometric curve shape
Liard River	52.8	0.6 %	Linear
Meade River	26.3	76 %	Concave, Convex
Sagavanirktok River	90.3	8.7 %	Linear
Tanana River at Fairbanks - Upstream	341	33 %	Convex, Concave
Tanana River at Fairbanks - Downstream	187	28 %	Linear
Tanana River at Nenana	44.9	38 %	Concave, Convex

hypsometric curve variability is to compute how much the slope of each sub-domain varies from the mean, weighted by the relative size of each sub-domain: the calculation for this quantity is given in Appendix A. By this metric, the Tanana River at Fairbanks Upstream has a variability of 33 %. In contrast, the Liard River has very low within-reach variability (<1 %). The river with the greatest within-reach hypsometric curve variability (76 %) is the Meade River, which has a steep section (53 m/m), then a flat section (3.5 m/m), and an intermediate section (25.9 m/m). Note that for the Meade satellite pass at highest WSE, the constrained and unconstrained datapoints fall essentially on top of each other. The other four reaches have variability between 9 % and 38 %.

Finally, we look at the shapes of the hypsometric curves. We classify the three “low variability” rivers (see previous paragraph) as having a linear shape. The Meade River hypsometric curve is neither fully concave nor fully convex but is a compound shape: it has first a concave section, and then a convex section. Note that the datapoint on the Meade corresponding to the highest flow is one where the constrained and unconstrained height and width are identical. The Tanana River at Nenana has a similar shape to the Meade River. In contrast, the Tanana River at Fairbanks Upstream reach has a shape that is first convex, and then concave. In summary, the simultaneous ArcticDEM WSE and width measurements reveal river hypsometry shapes with significant hypsometric slope variability between rivers, and within each reach, and with complex hypsometric curve shapes.

### 5.2. Height accuracy

Satellite WSE measurements at the six reaches accurately track in situ gage observations. Fig. 10 shows the comparison of both constrained and unconstrained WSE for each reach versus in situ stage for all six river reaches, and Table 4 provides corresponding standard deviations and correlation coefficients. The satellite observations capture the in situ observations in WSE, but with significant scatter. In some cases, e.g., the Liard River, the constrained WSE is visibly more precise than the unconstrained. Note that the stage measurements are relative to a local datum, and the WSE is relative to WGS84. After removing the bias, most satellite WSE measurements fall within 25 cm of the gage data with several outliers of ~100 cm. For the Tanana River at Fairbanks – Downstream, height RMSE is 33.4 cm (Table 4), consistent with Dai et al. (2018); the MAE is 23.3 cm and is more representative of a “typical” error because this metric is less sensitive to outliers. Note that the same gage is used for both Tanana River at Fairbanks Upstream and Downstream data, which is consistent with assuming that the water surface slope over this part of the river is constant in time, and thus the gage anomalies are similar in the two areas.

Across all six reaches, height performance varies substantially. From Table 4, error standard deviations of the unconstrained data vary from 18.1 cm (Meade River) to 48.7 cm (Tanana River at Nenana), with a median of 39.2 cm. The correlation coefficient ranges from 0.929 (Liard River) to 0.545 (Tanana River at Nenana). The hypsometrically constrained data improve in five of the six cases. The biggest improvement is for the Tanana River at Nenana, where the standard deviation in WSE improves from 48.7 cm to 33.9 cm and the correlation coefficient from 0.545 to 0.724. The only case of degradation is on the Meade River, where the WSE error standard deviation increases from 18.1 cm to 21.5 cm (19 %) and correlation coefficient drops from 0.931 to 0.900. Note that the Meade is also the river for which there are the fewest observations (10). The median accuracy for the constrained data is 33.4 cm, which is 5.8 cm lower than the median for the unconstrained data. Thus, the hypsometric constraint generally improves WSE performance, and there is generally more improvement for the lower precision WSE measurements.

### 5.3. Discharge accuracy

Fig. 11 shows example discharge hydrographs for the power law

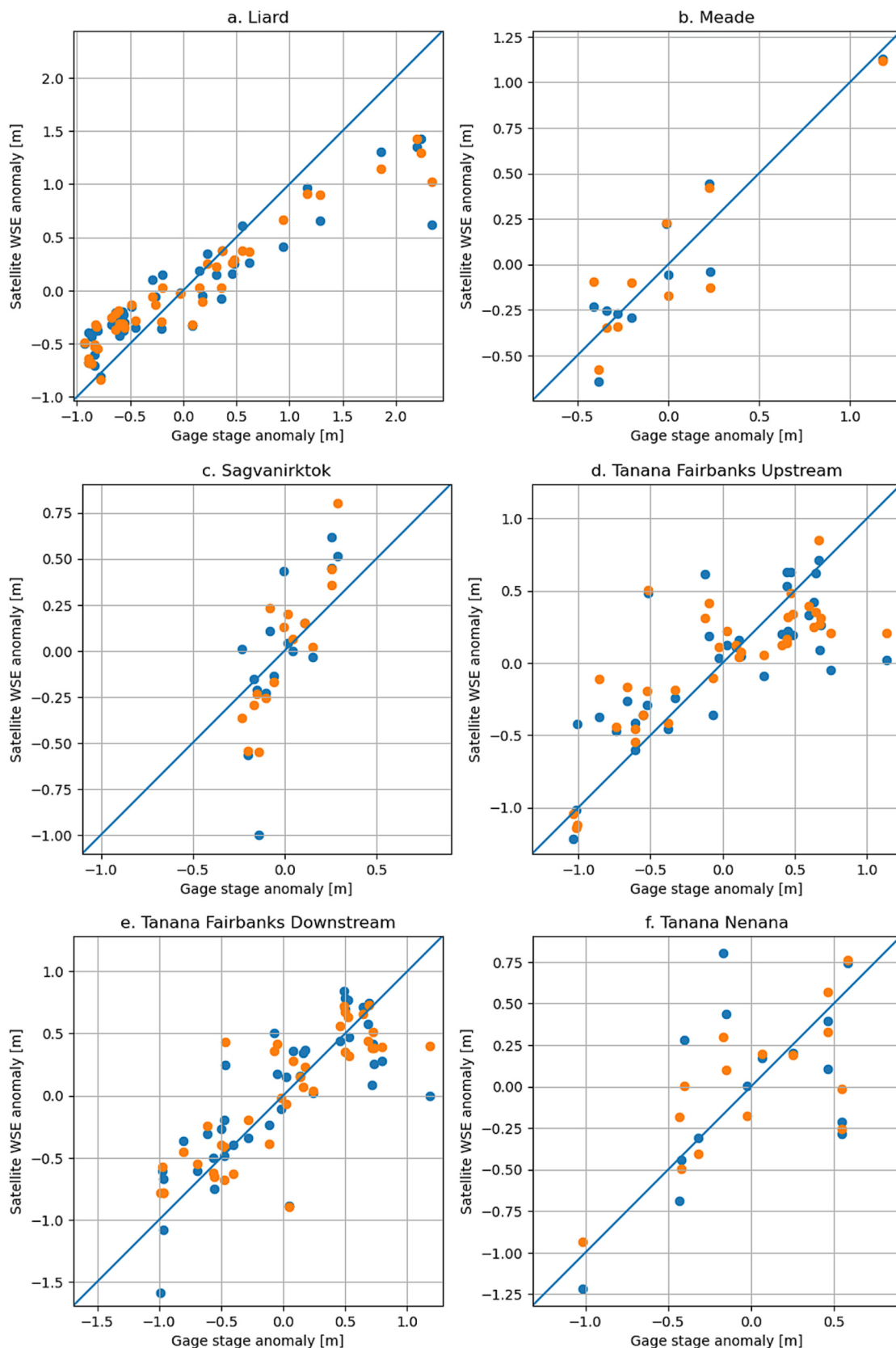


**Fig. 10.** Unconstrained (blue) and constrained (orange) scatterplots of ArcticDEM satellite observations of WSE compared with in situ stage measurements. In all cases, the x- and y- axis limits are the same. The mean value of each dataset has been removed, and thus the anomalies are presented here. (For interpretation of the references to colour in this figure legend, the reader is referred to the web version of this article.)

**Table 4**

WSE validation error statistics. The number of observations represents combined multispectral and panchromatic observations; the number of panchromatic observations is given in parentheses.

River Name	Number of Observations	Unconstrained $\sigma$ [cm]	Constrained $\sigma$ [cm]	Unconstrained r	Constrained r
Liard River	44 (0)	45.2	40.0	0.929	0.964
Meade River	10 (3)	18.1	21.5	0.931	0.900
Sagavanirkto River	16 (3)	31.1	23.7	0.726	0.878
Tanana River at Fairbanks - Upstream	36 (0)	40.0	36.9	0.741	0.785
Tanana River at Fairbanks - Downstream	40 (0)	38.5	33.0	0.781	0.832
Tanana River at Nenana	15 (13)	48.7	33.9	0.545	0.724

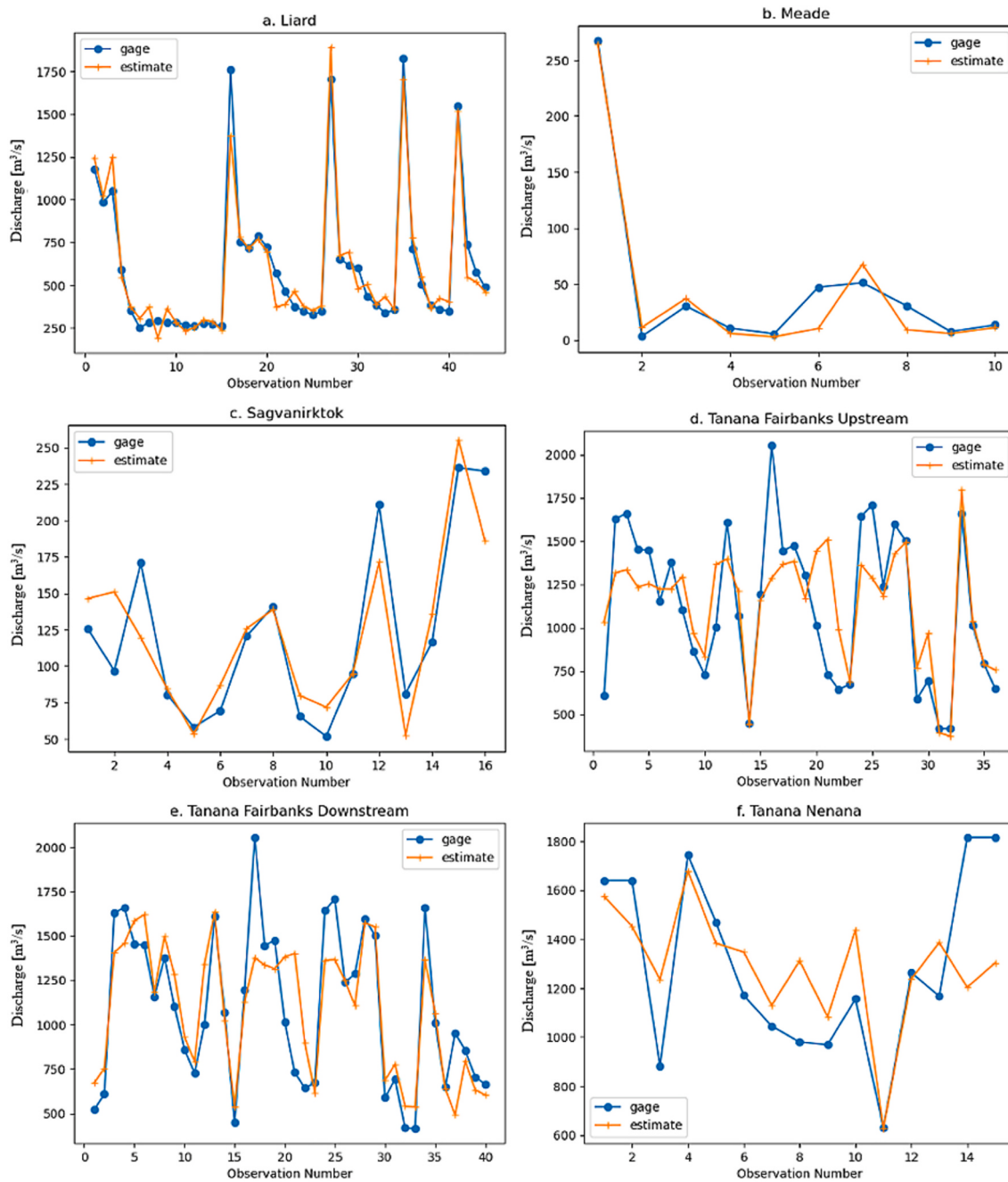


**Fig. 11.** Example discharge results for the power law friction coefficient flow law (combining Eqs. 22 and 23) for each river reach.

friction coefficient flow law (Eqs. 23a and 23b) for all six reaches using the constrained heights and widths. The timeseries is arranged in chronological order, but the horizontal axis represents the observation number in the sequence rather than actual time. Recall that the period

spans approximately twelve years for gages that include WorldView-1 results and the observations are arbitrarily spaced within that period, based on when satellite operators chose to acquire particular scenes. The Liard (Fig. 11a) shows seasonal cycles for some years. Similar to the WSE

results, remotely sensed discharge tends to track the gaged values. Outliers visually play an important role. Qualitatively, there is not a significant difference between the accuracy of the high and low flows as compared with average flows; e.g., both high flows and low flows are captured fairly accurately on the Liard and Meade Rivers. The Tanana River at Nenana appears to perform the worst in capturing the high and low flow, while both reaches of the Tanana at Fairbanks underestimate some of the high flow peaks.

Three error metrics adequately describe discharge accuracy: nRMSE, nMAE, and KGE. The nMAE is significantly less than nRMSE in many (though not all) cases. For example, for the Tanana at Fairbanks Downstream, the power law friction coefficient flow law has nRMSE of 0.21 and nMAE of 0.15. The reason for this can be seen in Fig. 11, where most of the high flows are underestimated, leading the nRMSE metric to

be governed by these infrequent values. We show nMAE and nRMSE throughout, as both capture important aspects of performance. In general, low values of error (e.g.,  $nRMSE < 0.25$ ) correspond to high values of efficiency (e.g.,  $KGE > 0.5$ ). However, for the Tanana River at Nenana, this is not the case. From Fig. 11, we infer that this is in part because the gaged flows vary less than in other rivers, meaning that the discharge errors can be relatively small, even though the variability in the gage timeseries is not well represented by the remotely sensed estimates. Note that the gaged variability itself is a function more of when images are available for each river than intrinsic hydrologic variability.

For most rivers, error is quite consistent across most flow laws, with few exceptions (Fig. 12). The Meade shows that AHG for width (Eq. 19) performs poorly compared to formulations that use WSE. In the case of the Meade, there is simply not a very strong relationship between

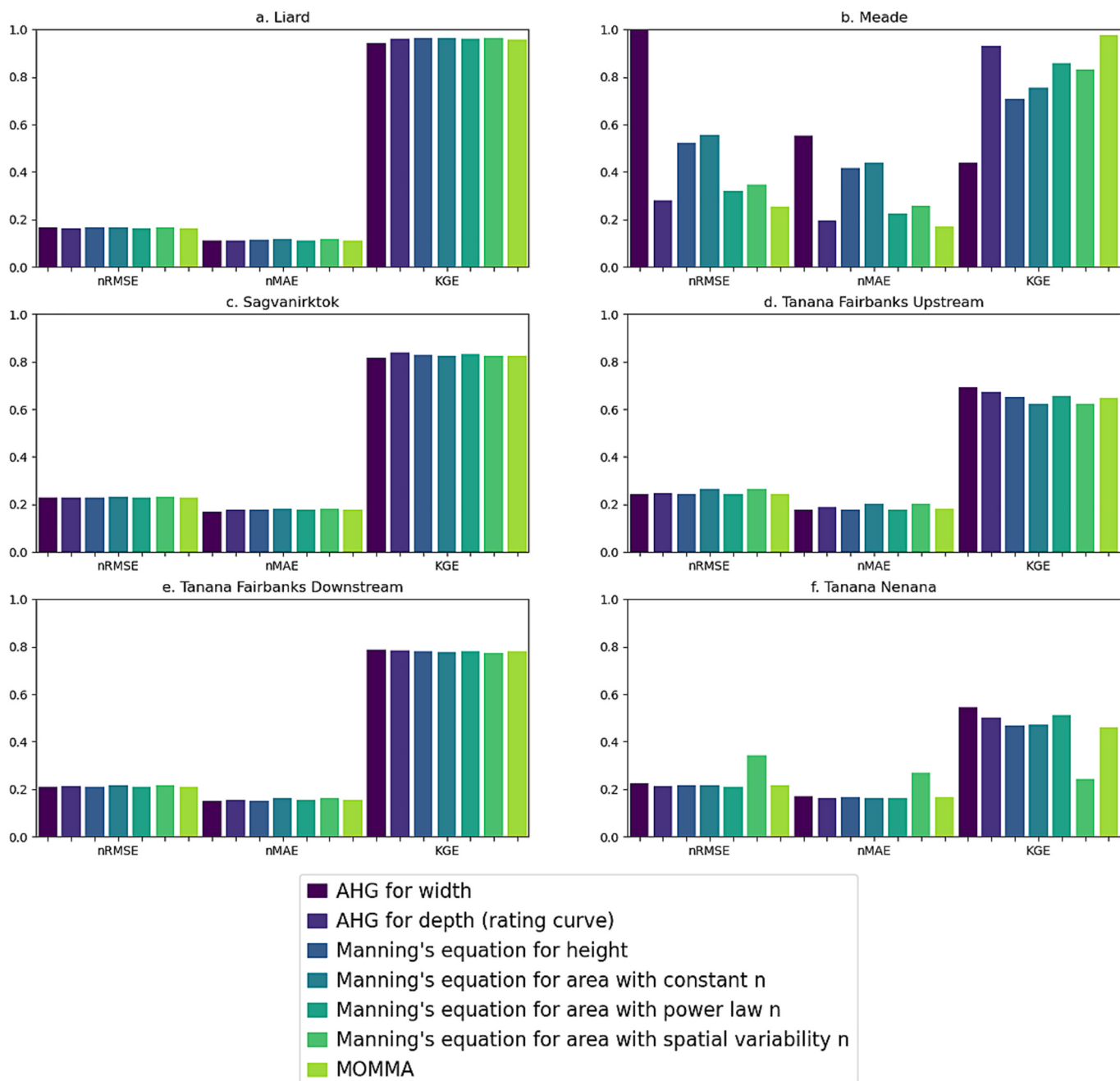


**Fig. 12.** Bar plots showing comparisons of flow law accuracies (shown as different colors) for each river reach (corresponding to the six subplots) and for three error metrics. The nRMSE bar for the Meade River AHG for width extends off the chart and is equal to 1.28.

remotely sensed width and gage discharge data (Figure S-2). One reason for this may be that the variability of remotely sensed width (ranging from 125 m to 175 m) is small compared to the width measurement precision. AHG for width (Eq. 19) performs worst, while AHG for depth (Eq. 20) does nearly the best. The estimated hydrographs for comparison flow laws are shown in Figure S-2 for the Meade. Presumably, this is simply a case of poor width or discharge observations and low sample size. In summary, discharge performance is fairly consistent across flow laws, with erratic performance on the Meade river with low sample size and a poor relationship between unconstrained width and discharge.

#### 5.4. Effect of height-width constraint on discharge accuracy

Constraining height and width measurements to the hypsometric

curve is expected to reduce uncertainty in discharge (Section 2.3). In this section, we explore the effect of the height-width constraint by comparing discharge accuracy results with and without the constraint. Fig. 13 shows that the height-width constraint significantly improves discharge accuracy in almost every case. Improvements are significant for some rivers: nRMSE is reduced by nearly 0.1 (i.e., from 0.3 to 0.2) for most flow laws on the Liard River. The KGE metric improves significantly for five of the seven flow laws on the Tanana at Nenana, showing that WSE and width measurements together help to improve the ability to track discharge variations. Visually, there is far more variability among flow laws when no height-width constraint is performed; this is especially evident on the Tanana River at Fairbanks Downstream (compare Fig. 13 and Figure S-3). The Meade River discharge accuracy is improved in most cases, especially for the width-based flow laws,

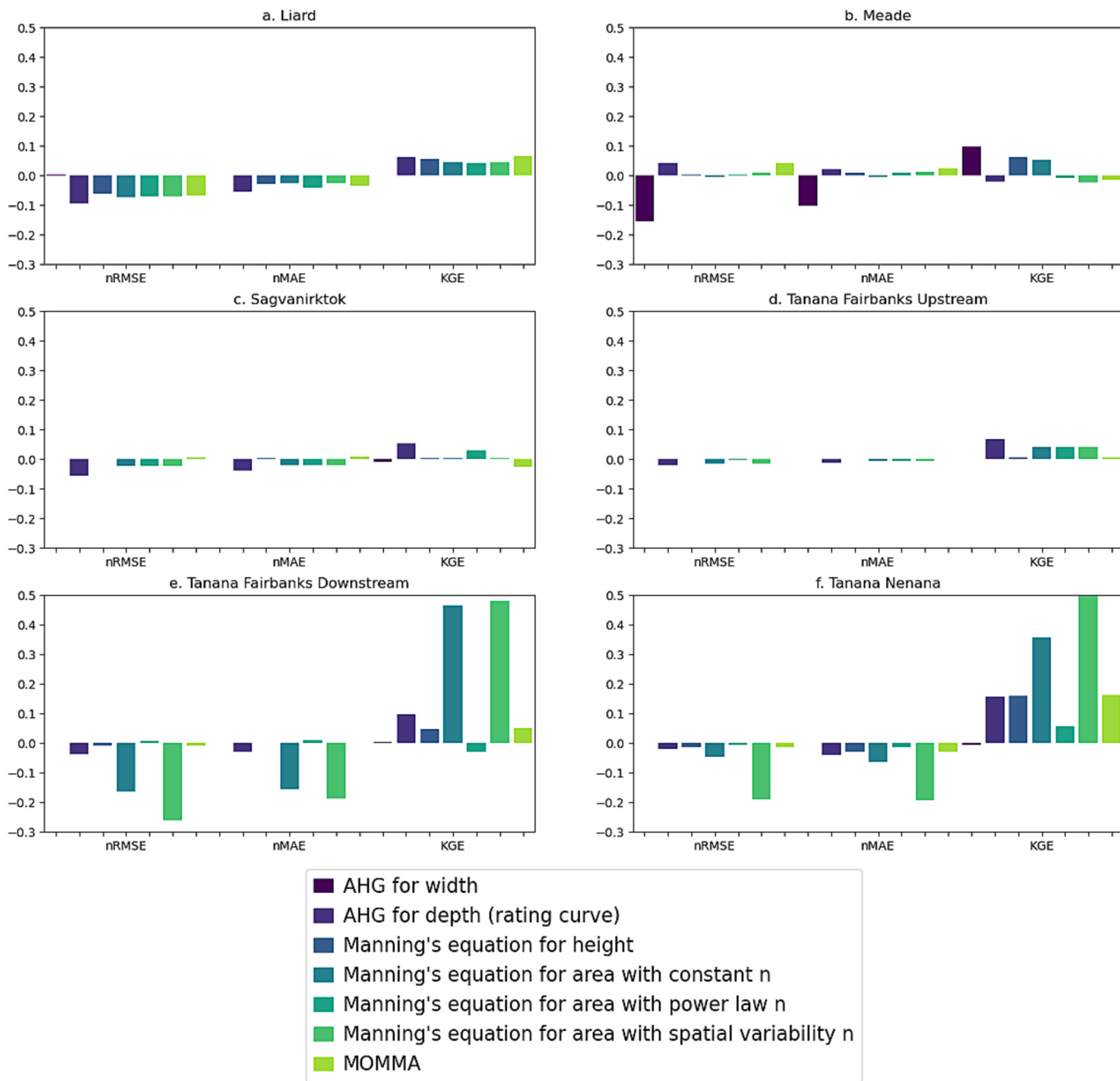


**Fig. 13.** The effect of the height-width constraint on discharge accuracy is shown. The plots show the difference in error metrics with and without the height-width constraint. In these plots, negative values for nRMSE and nMAE and positive values for KGE indicate that the height-width constraint improves discharge accuracy. The improvement in KGE for the Tanana River at Nenana extends off the edge of the graphic, and is equal to 0.759.

despite the fact that WSE accuracy is slightly degraded (as shown previously). Indeed, the largest degradation on the Meade is for the AHG for depth flow law, the only flow law that does not use width. There are very slight degradations in discharge performance on the Meade River for some flow laws, but not nearly as large as the improvements to e.g., the AHG for the width flow law. These degradations largely vanish if the analysis is re-run using a higher specified width uncertainty (15 m compared with the nominal value of 5 m) for the Meade River (not shown). Meade River widths likely were measured less precisely than initially hypothesized, and specifying a precision higher than the true value led to this slight degradation in WSE and discharge accuracy. This result highlights the importance of using accurate width and WSE uncertainty values. In summary, across all sites, the height-width constraint improves discharge accuracy.

## 6. Conclusions

In this paper, we present measurements of river hypsometry, available via simultaneous WSE and width measurements from high spatial resolution commercial imagery. We describe a method to estimate river hypsometric curves as piecewise-linear relationships between river width and WSE from noisy satellite observations. We also present a method to constrain width and WSE measurements to the river hypsometric curve and demonstrate that hypsometrically constrained WSE and width measurements show improved precision, at the expense of correlation among WSE and width errors. We demonstrate that discharge estimated with hypsometrically constrained WSE and width shows improved precision, by analyzing a stochastic model of discharge uncertainty given WSE and width uncertainty and their correlation, and through a Monte Carlo numerical experiment. We find that expected improvement in discharge accuracy is a function of relative WSE and width measurement precision. The numerical experiment predicts that discharge should be significantly improved by using constrained height and width measurements with the high-resolution commercial imagery used in the study, and that the same approach will be valuable (but not as impactful) with SWOT measurements given their expected WSE and width uncertainty.

We find significant variability among the river hypsometric curves over the study area: the average slope of the hypsometric curves varied by over an order of magnitude from a minimum of 26.3 m change in width per meter change in WSE (m/m) on the Meade River to a maximum of 341 m/m on the Tanana River at the Fairbanks upstream reach. We find that WSE accuracy ranges from 18.1 to 48.7 cm (median 39.3 cm), and that applying the hypsometric constraint improves accuracy in five of the six cases, improving the median performance to 33.4 cm. Moreover, the hypsometric constraint improves discharge accuracy and consistency: constrained height and width produce more accurate discharge estimates and show fewer variations among flow laws. One caveat of the analysis presented here is that the same set of WSE and width observations were used to compute the hypsometric curve and to evaluate discharge accuracy. Future work should explore the effect of applying hypsometric curves to data not used in their calibration. Our results show that when width uncertainty was underestimated (on the Meade River), the constraint actually degraded discharge performance somewhat. We recommend that the forthcoming SWOT mission adopt a similar strategy and compute height-width constrained measurements, once WSE and width uncertainty estimates have been validated.

The results presented here help shed light on the state of the art and future of remote sensing of river discharge (Durand et al., 2023). The datasets presented here advance our ability to resolve river elevations and width spatially and provide simultaneous measurements of WSE and

width. Most available remote sensing instruments can measure either WSE or width, but not both from the same platform. As remote sensing of rivers evolves, a major leap forward is expected as we transition from remote sensing of WSE from a single profile across rivers to methods that resolve WSE spatially and at high precision. Most currently available remotely sensed measurements of WSE provide a profile, yielding on the order of  $10^1$  observations over a river cross-section, and do not provide adequate data to average over noisy river processes. The method and datasets presented here resolves water surface elevation along both river shorelines at 2 m resolution, and filters out many raw datapoints, amounting to on the order of  $10^2$  observations per river kilometer. SWOT will resolve the river, not the shorelines, and thus will provide on the order of  $10^3$  observations per kilometer on a 100 m wide river. This transition to dense spatial coverage will also enable more precise river slope observations. Datasets presented here thus provide something far closer to SWOT-like data compared to conventional altimetry, though they are still significantly less precise. Our findings provide support for applying river hypsometry constraints to improve WSE and width precision for discharge estimates from SWOT (Durand et al., 2023).

## CRediT authorship contribution statement

**Michael Durand:** Writing – review & editing, Writing – original draft, Visualization, Validation, Supervision, Software, Resources, Project administration, Methodology, Investigation, Funding acquisition, Formal analysis, Conceptualization. **Chunli Dai:** Software, Data curation, Conceptualization. **Joachim Moortgat:** Software, Methodology, Data curation. **Bidhyananda Yadav:** Writing – review & editing, Software, Data curation. **Renato Prata de Moraes Frasson:** Resources, Investigation, Conceptualization. **Ziwei Li:** Resources, Data curation. **Kylie Wadkowsky:** Resources, Investigation. **Ian Howat:** Resources, Methodology, Investigation, Conceptualization. **Tamlin M. Pavelsky:** Resources, Investigation.

## Declaration of competing interest

The authors declare that they have no known competing financial interests or personal relationships that could have appeared to influence the work reported in this paper.

## Data availability

The authors are unable or have chosen not to specify which data has been used.

## Acknowledgments

The authors would like to acknowledge funding from NASA Terrestrial Hydrology Program grant 80NSSC18K1497. Geospatial support for this work provided by the Polar Geospatial Center under NSF-OPP awards 1043681 and 1559691. DEMs provided by the Polar Geospatial Center under NSF-OPP awards 1043681, 1559691, and 1542736. Renato Frasson would like to acknowledge funding received through the SWOT Science Team proposal number 19-SWOTST19-0020. A portion of this work was performed at the Jet Propulsion Laboratory, California Institute of Technology, under contract with NASA. Calculations done by the Flow Law Parameter Estimation libraries designed at Byrd Polar (FLaPE-Byrd) available at <https://github.com/mikedurand/FLaPE-Byrd>. Thanks to Nikki Tebaldi (University of Massachusetts, Amherst) for assistance designing FLaPE-Byrd. Thanks to Haylen Scott for graphical design on Fig. 1.

## Appendix A. Calculation of the variability of river hypsometric slope

The methods above specify three sub-domains for each reach, defined by breakpoints in the piecewise linear relationship. The average slope of the river hypsometric curve (and thus the average response of river width to WSE) can be calculated by simply computing the change in width and dividing by change in WSE, using the first and last breakpoint. The exact same value of the average river hypsometry slope  $\overline{S_{HW}}$  can also be calculated using a kind of weighted average:

$$\overline{S_{HW}} = \sum_{i=1}^3 P_i S_{HW,i} \quad (\text{A-1})$$

where the summation is over the three subdomains,  $S_{HW,i}$  is the river hypsometry slope of subdomain  $i$ , and  $P_i$  is the weight given to each subdomain, and is computed based on the WSE breakpoints using:

$$P_1 = \frac{H_0 - H_{min}}{H_{max} - H_{min}} \quad (\text{A-2})$$

where  $H_0$  is the first of two breakpoints defining the three sub-domains, and  $H_{min}$  and  $H_{max}$  define the maximum and minimum values of the entire domain, respectively (e.g., the minimum and maximum measured WSE values). Note that  $P_1 + P_2 + P_3 = 1$ . This form can be extended to compute a variance of the slopes over the three sub-domains, where the  $P_i$  values are interpreted as the probability mass in each subdomain:

$$\sigma_{HW}^2 = \sum_{i=1}^3 P_i (S_{HW,i} - \overline{S_{HW}})^2 \quad (\text{A-3})$$

The values of variability in Table 3 are coefficients of variation (i.e.,  $\sigma_{HW}/\overline{S_{HW}}$ ). We compared these values to the range (difference of the maximum and minimum slope) divided by the mean slope and obtained qualitatively similar values.

## Appendix B. Supplementary data

Supplementary data to this article can be found online at <https://doi.org/10.1016/j.rse.2024.114455>.

## References

- Altenau, E.H., Pavelsky, T.M., Moller, D., Pitcher, L.H., Bates, P.D., Durand, M.T., Smith, L.C., 2019. Temporal variations in river water surface elevation and slope captured by AirSWOT. *Remote Sens. Environ.* 224, 304–316. <https://doi.org/10.1016/j.rse.2019.02.002>.
- Altenau, E.H., Pavelsky, T.M., Durand, M.T., Yang, X., Frasson, R.P.D., Bendezu, L., 2021. The surface water and ocean topography (SWOT) Mission River database (SWORD): a Global River network for satellite data products. *Water Resour. Res.* 57, e2021WR030054. <https://doi.org/10.1029/2021wr030054>.
- Bjerkie, D.M., Birkett, C.M., Jones, J.W., Carabajal, C., Rover, J.A., Fulton, J.W., Garambois, P.A., 2018. Satellite remote sensing estimation of river discharge: application to the Yukon River Alaska. *J. Hydrol.* 561, 1000–1018. <https://doi.org/10.1016/j.jhydrol.2018.04.005>.
- Coss, S., Durand, M., Yi, Y.C., Jia, Y.Y., Guo, Q., Tuozzolo, S., Shum, C.K., Allen, G.H., Calmant, S., Pavelsky, T., 2020. Global River radar altimetry time series (GRRATS): new river elevation earth science data records for the hydrologic community. *Earth System Science Data* 12, 137–150. <https://doi.org/10.5194/essd-12-137-2020>.
- Coss, S., Durand, M.T., Shum, C.K., Yi, Y.C., Yang, X., Pavelsky, T., Getirana, A., Yamazaki, D., 2023. Channel water storage anomaly: a new remotely sensed quantity for Global River analysis. *Geophys. Res. Lett.* 50, e2022GL100185. <https://doi.org/10.1029/2022gl100185>.
- Cretaux, J.F., Biancamaria, S., Arsen, A., Berge-Nguyen, M., Becker, M., 2015. Global surveys of reservoirs and lakes from satellites and regional application to the Syrdarya river basin. *Environ. Res. Lett.* 10, 015002. <https://doi.org/10.1088/1748-9326/10/1/015002>.
- Dai, C.L., Durand, M., Howat, I.M., Altenau, E.H., Pavelsky, T.M., 2018. Estimating river surface elevation from ArcticDEM. *Geophys. Res. Lett.* 45, 3107–3114. <https://doi.org/10.1002/2018gl077379>.
- Durand, M., Gleason, C.J., Garambois, P.A., Bjerkie, D., Smith, L.C., Roux, H., Rodriguez, E., Bates, P.D., Pavelsky, T.M., Monnier, J., Chen, X., Di Baldassarre, G., Fiset, J.M., Flipo, N., Frasson, R., Fulton, J., Goutal, N., Hossain, F., Humphries, E., Minear, J.T., Mukolwe, M.M., Neal, J.C., Ricci, S., Sanders, B.F., Schumann, G., Schubert, J.E., Vilmin, L., 2016. An intercomparison of remote sensing river discharge estimation algorithms from measurements of river height, width, and slope. *Water Resour. Res.* 52, 4527–4549. <https://doi.org/10.1002/2015wr018434>.
- Durand, M., Gleason, C.J., Pavelsky, T.M., Frasson, R.P.D., Turmon, M., David, C.H., Altenau, E.H., Tebaldi, N., Larnier, K., Monnier, J., Malaterre, P.O., Oubanas, H., Allen, G.H., Astifan, B., Brinkerhoff, C., Bates, P.D., Bjerkie, D., Coss, S., Dudley, R., Fenoglio, L., Garambois, P.A., Getirana, A., Lin, P.R., Margulies, S.A., Matte, P., Minear, J.T., Muhebwa, A., Pan, M., Peters, D., Riggs, R., Sikder, M.S., Simmons, T., Stuurman, C., Taneja, J., Tarpanelli, A., Schulze, K., Tourian, M.J., Wang, J.D., 2023. A framework for estimating Global River discharge from the surface water and ocean topography satellite Mission. *Water Resour. Res.* 59. <https://doi.org/10.1029/2021wr031614>.
- Frasson, R.P.D., Durand, M.T., Larnier, K., Gleason, C., Andreadis, K.M., Hagemann, M., Dudley, R., Bjerkie, D., Oubanas, H., Garambois, P.A., Malaterre, P.O., Lin, P.R., Pavelsky, T.M., Monnier, J.M., Brinkerhoff, C.B., David, C.H., 2021. Exploring the factors controlling the error characteristics of the surface water and ocean topography Mission discharge estimates. *Water Resour. Res.* 57. <https://doi.org/10.1029/2020wr028519>.
- Fuller, W.A., 1987. *Measurement error models*. John Wiley & Sons, New York.
- Gleason, C.J., Durand, M.T., 2020. Remote sensing of river discharge: a review and a framing for the discipline. *Remote Sens.* 12. <https://doi.org/10.3390/rs12071107>.
- Hannah, D.M., Demuth, S., van Lanen, H.A.J., Looser, U., Prudhomme, C., Rees, G., Stahl, K., Tallaksen, L.M., 2011. Large-scale river flow archives: importance, current status and future needs. *Hydrol. Process.* 25, 1191–1200. <https://doi.org/10.1002/hyp.7794>.
- Isikdogan, L.F., Bovik, A., Passalacqua, P., 2020. Seeing through the clouds with DeepWaterMap. *IEEE Geosci. Remote Sens. Lett.* 17, 1662–1666. <https://doi.org/10.1109/lgrs.2019.2953261>.
- IUGLS, 2009. Impacts on Upper Great Lakes Water Levels: St. Clair River, Final report to the International Joint Commission. <http://www.ijc.org>.
- Leopold, L.B., Maddock, T., 1953. *The Hydraulic Geometry of Stream Channels and some Physiographic Implications*. Geological Survey Professional Paper, Washington.
- Moortgat, J., Li, Z.W., Durand, M., Howat, I., Yadav, B., Dai, C.L., 2022. Deep learning models for river classification at sub-meter resolutions from multispectral and panchromatic commercial satellite imagery. *Remote Sens. Environ.* 282, 113279. <https://doi.org/10.1016/j.rse.2022.113279>.
- Noh, M.J., Howat, I.M., 2015. Automated stereo-photogrammetric DEM generation at high latitudes: surface extraction with TIN-based search-space minimization (SETSM) validation and demonstration over glaciated regions. *Gisci. Remote Sens.* 52, 198–217. <https://doi.org/10.1080/15481603.2015.1008621>.
- Noh, M.J., Howat, I.M., 2017. The surface extraction from TIN based search-space minimization (SETSM) algorithm. *ISPRS J. Photogramm. Remote Sens.* 129, 55–76. <https://doi.org/10.1016/j.isprsjprs.2017.04.019>.
- Porter, C., Howat, I., Noh, M., Husby, E., Khuvivs, S., Danish, E., Tomko, K., Gardiner, J., Negrete, A., Yadav, B., 2022. ArcticDEM-strips, version 4.1. *Harvard Dataverse*, 1.
- Rodriguez, E., Durand, M., Frasson, R.P.D., 2020. Observing Rivers with varying spatial scales. *Water Resour. Res.* 56, e2019WR026476. <https://doi.org/10.1029/2019wr026476>.
- Schwenk, J., Khandelwal, A., Fratkin, M., Kumar, V., Foufoula-Georgiou, E., 2017. High spatiotemporal resolution of river planform dynamics from Landsat: the RivMAP toolbox and results from the Ucayali River. *Earth Space Sci.* 4, 46–75. <https://doi.org/10.1020/2016ea000196>.
- Stuurman, C., Pottier, C., Chen, C., Fjortoft, R., Kwoun, O.-I., Vadon, H., 2022. Surface Water and Ocean Topography (SWOT) Project SWOT Product Description: Level 2 KaRIn High Rate River Single Pass Vector Product (L2\_HR\_RiverSP). California

Institute of Technology. Available online: <https://podaac.jpl.nasa.gov/SWOT?tab=datasets&sections=about%2Bdata>.

Tortini, R., Noujdina, N., Yeo, S., Ricko, M., Birkett, C.M., Khandelwal, A., Kumar, V., Marlier, M.E., Lettenmaier, D.P., 2020. Satellite-based remote sensing data set of global surface water storage change from 1992 to 2018. *Earth System Science Data* 12, 1141–1151. <https://doi.org/10.5194/essd-12-1141-2020>.

Tuozzolo, S., Langhorst, T., Frasson, R., Pavelsky, T., Durand, M., Schobelock, J.J., 2019. The impact of reach averaging Manning's equation for an in-situ dataset of water surface elevation, width, and slope. *J. Hydrol.* 578, 123866. <https://doi.org/10.1016/j.jhydrol.2019.06.038>.